



GEORG-AUGUST-UNIVERSITÄT  
GÖTTINGEN

Fakultät für  
Physik 

**Bachelor's Thesis**

**Analyse von Produktionsmessungen  
mit Modulen des  
ATLAS-Pixeldetektors**

**Analysis of production measurements  
with modules of the ATLAS Pixel  
Detector**

II.Physik-UniGö-Bach-2009/05

prepared at the II. Physikalisches Institut  
by Lars Graber from Göttingen

**Thesis period:** 14th April 2009 until 21st July 2009

**Supervisor:** PD Dr. Jörn Große-Knetter

**First referee:** Prof. Dr. Arnulf Quadt

**Second referee:** PD Dr. Jörn Große-Knetter



## **Abstract**

This thesis is about the readout electronics of the ATLAS Pixel Detector.

In the first part methods to detect unconnected bump bonds are compared. This is done because the most reliable method, the source scan, is not available for modules built in the detector. The result is that using measured noise from the threshold scan can provide an alternative method. However, not all defect bump bonds can be detected.

In the second part a new function for the relation between ToT and deposit charge from a particle is tested against the currently used one. Although the new function is derived from the theoretical shape of the charge pulse, it proves to be less accurate.

**Keywords:** Physics, Bachelor thesis, ATLAS, Pixel Detector



# Contents

<b>1</b>	<b>Introduction</b>	<b>1</b>
1.1	Overview . . . . .	1
1.2	LHC and ATLAS . . . . .	1
<b>2</b>	<b>The ATLAS Pixel Detector</b>	<b>3</b>
2.1	Physical principle of a semiconductor detector . . . . .	4
2.1.1	Energy loss of particles in matter . . . . .	4
2.1.2	Charge collection and noise . . . . .	6
2.2	The Pixel module . . . . .	7
2.2.1	The Front-End chip . . . . .	8
2.2.2	Bump bond connections . . . . .	10
2.2.3	Testing and production stages of the modules . . . . .	11
<b>3</b>	<b>The ATLAS Trigger System</b>	<b>13</b>
<b>4</b>	<b>Analysis of bump bond connection quality</b>	<b>15</b>
4.1	Module tests . . . . .	15
4.1.1	Source scan . . . . .	15
4.1.2	Noise from threshold scan . . . . .	16
4.2	Computational analysis of test data . . . . .	16
4.3	Results . . . . .	17
4.3.1	Results from the source scan . . . . .	17
4.3.2	Results from the threshold scan with depleted sensor . . . . .	20
4.3.3	Results from the threshold scan with undepleted sensor . . . . .	24
4.3.4	Combined results . . . . .	26
4.3.5	Correlation between ASSY and FLEX . . . . .	28
4.4	Merged bump bonds . . . . .	28
<b>5</b>	<b>Time over threshold analysis</b>	<b>31</b>

*Contents*

5.1	Measurement of the ToT . . . . .	33
5.2	Computational analysis of test data . . . . .	33
5.3	Results . . . . .	35
5.3.1	Module 510064 at FLEX stage . . . . .	35
5.3.2	Module 510064 at other stages . . . . .	37
<b>6</b>	<b>Conclusion</b>	<b>39</b>
6.1	Analysis of bump bond connection quality . . . . .	39
6.2	Time over threshold analysis . . . . .	40

# Nomenclature

$v$	velocity	m/s
$c$	speed of light	m/s
$\beta$	$v/c$	
$\gamma$	$(1 - \beta)^{-1/2}$	
LHC	Large Hadron Collider	
ID	inner detector	
BCU	bunch crossing unit	25 ns
m.i.p.	minimum ionising particle	
ToT	time over threshold	BCU
FE chip	front-end chip	
DAC	digital-analogue converter	
ENC	equivalent noise charge	

## *Nomenclature*

# 1 Introduction

## 1.1 Overview

In this thesis methods of detecting unconnected bump bond connections and functions for the relation between ToT and deposit charge are discussed.

After a brief introduction to LHC and ATLAS (chapter 1.2) the physical principles of a semiconductor detector are described (chapter 2.1). In chapter 2.2 the operating mode of the modules of the ATLAS Pixel Detector is explained. A short explanation of the ATLAS trigger system will be covered in chapter 3. Chapter 4 will contain the different analysis methods for unconnected bump connections, as well as a description of the module tests used for the analysis (chapter 4.1). The different functions to fit the ToT data are discussed in chapter 5.

## 1.2 LHC and ATLAS

The LHC is a proton-proton collider at CERN, Geneva in Switzerland. It has a proposed center of mass energy of 14 TeV so that it should be able to produce the Higgs-boson and a design luminosity of  $10^{34} \text{ cm}^{-2}\text{s}^{-1}$ . Furthermore indications for new physics may be expected. Currently the estimated start of operation is November 2009.

The ATLAS detector, an acronym for A Toroidal LHC ApparatuS, is one of four main experiments at the LHC. It is a multi purpose detector. Some parameters of the detector are given in Tab. 1.1. As the accelerator will be run at 40 MHz and the high luminosity the detector electronics must be fast and radiation-hard. Other

height	25 m		weight	7000 t
length	44 m		$ \eta $	$\leq 4.9$

Table 1.1: Parameters of the ATLAS detector [1].

## 1 Introduction

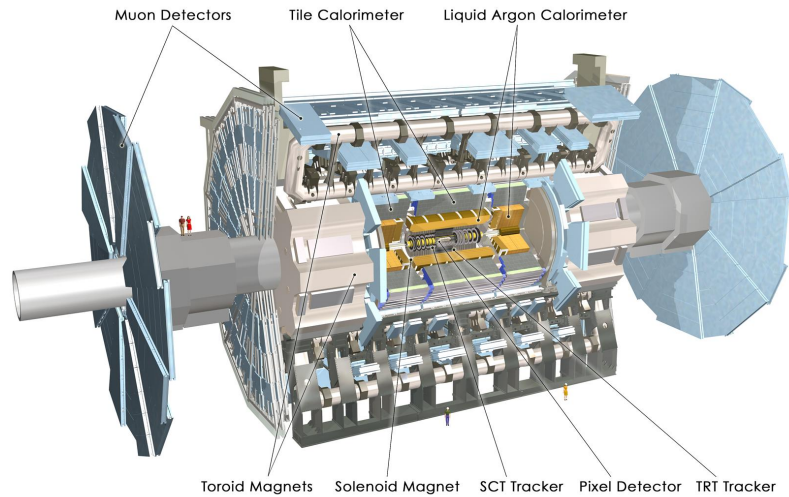


Figure 1.1: Schematic view of the ATLAS detector.

requirements are a high pseudorapidity  $\eta$  to detect as many particles as possible and a good momentum resolution near the interaction point for tagging  $b$ -jets and  $\tau$ -leptons. Very good calorimeters so that the missing energy is as low as possible and an excellent muon tracking system to measure the transverse momentum of high energy muons are also needed. To reduce the amount of data an efficient trigger system is installed (see Chapter 3) [1].

The schematic layout of the whole detector can be seen in Fig. 1.1. From the inner to the outer radius it consists of the inner detector (ID), electromagnetic and hadronic calorimeters and a muon tracking system. In addition there are two magnetic fields. Around the muon tracking system is a toroidal field with 0.5 T in the barrel region and 1 T in the end-caps. A solenoidal magnetic field with 2 T surrounds the ID. The ID itself consists of three parts: the Pixel Detector (see chapter 2.2) as the most inner one, the silicon microstrip tracker (SCT) in the middle and the transition radiation tracker (TRT) as the most outer one.

## 2 The ATLAS Pixel Detector

The ATLAS Pixel Detector is the innermost detector of ATLAS with a distance to the collision point between 50.5 mm and 149.6 mm radially and up to 650 mm along the beam pipe [1]. It consists of 1744 individual modules which are mounted on three barrel layers around the collision point and additionally on three end-cap discs in each direction. Thus a traversing particle up to a pseudo-rapidity of  $|\eta| < 2.5$  hits the detector at least three times and the momentum of the particle can be calculated via the Glückstern formula [2]. A drawing of the detector can be seen in fig 2.1. The structure on which the modules are mounted also serves as cooling device and cools the modules down to a temperature between  $-5\text{ }^{\circ}\text{C}$  and  $-10\text{ }^{\circ}\text{C}$  to reduce noise in the detector material and electronics. The sensor material is 250  $\mu\text{m}$  thick silicon which is divided into 47232 pixels on each module. Since some pixels are ganged with each other one obtains 46080 individual read-out channels per module resulting in over 80 million channels for the whole detector.

A description of the modules is given in Chapter 2.2. In Chapters 4 and 5 an analysis of these modules, precisely the pixels, is done.

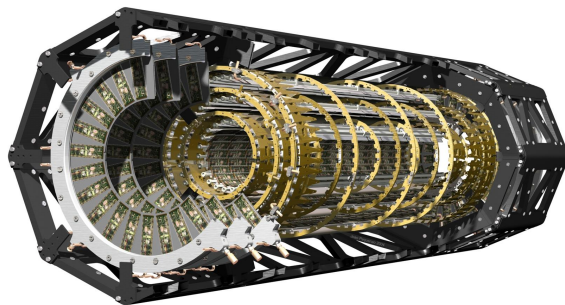


Figure 2.1: Schematic view of the ATLAS Pixel Detector.

## 2.1 Physical principle of a semiconductor detector

### 2.1.1 Energy loss of particles in matter

A particle traversing through matter interacts with it in different ways and loses thereby energy. The type of interaction depends on the type of the traversing particle. A charged one can interact in three different ways [3]:

- ionization or excitation
- cherenkov radiation
- transmission radiation in inhomogeneous materials

The main effect for most detectors as for the Pixel Detector is ionization. A traversing particle deposits hereby its energy in electron/ion- or electron/hole-pairs in gas or semiconductor, respectively. The amount of energy lost per distance for heavy charged particles, which means every charged particle except the electron, is described by the Bethe-Bloch formula [4]

$$-\left\langle \frac{dE}{dx} \right\rangle = 2\pi N_a r_e^2 m_e c^2 \rho \frac{Z}{A} \frac{z^2}{\beta^2} \left[ \ln \left( \frac{2m_e \gamma^2 v^2 W_{max}}{I^2} \right) - 2\beta^2 \right] \quad (2.1)$$

where  $r_e$  is the classical electron radius,  $m_e$  the electron mass,  $N_a$  Avogadro's number,  $I$  the mean excitation potential,  $Z$  the atomic number of the absorbing material,  $A$  its atomic weight and  $\rho$  its density,  $z$  the charge of the incident particle and  $W_{max}$  the maximum energy transfer in a single collision.

The whole formula can be written as a function of  $\beta\gamma$  as shown in Fig. 2.2 for a muon. One can notice that the Bethe-Bloch formula only applies for  $0.08 < \beta\gamma < 800$ . For a value of  $\beta\gamma \approx 3 \dots 4$ , the energy loss has a minimum which belongs to a value of  $\left\langle \frac{dE}{dx} \right\rangle = 1.5 \frac{\text{MeV}}{\text{g cm}^{-2}}$ . Those particles are called minimum ionizing particles (m.i.p.). This value is often used to calibrate a detector, because it is the minimal energy a detector should recognize.

The ATLAS Pixel Detector uses 250  $\mu\text{m}$  thick silicon with a density of  $2.33 \text{ g cm}^{-3}$  as sensor material. So a vertically passing m.i.p. loses

$$\langle \Delta E \rangle = 1.5 \frac{\text{MeV}}{\text{g cm}^{-2}} \cdot 2.33 \text{ g cm}^{-3} \cdot 250 \mu\text{m} = 87 \text{ keV}$$

## 2.1 Physical principle of a semiconductor detector

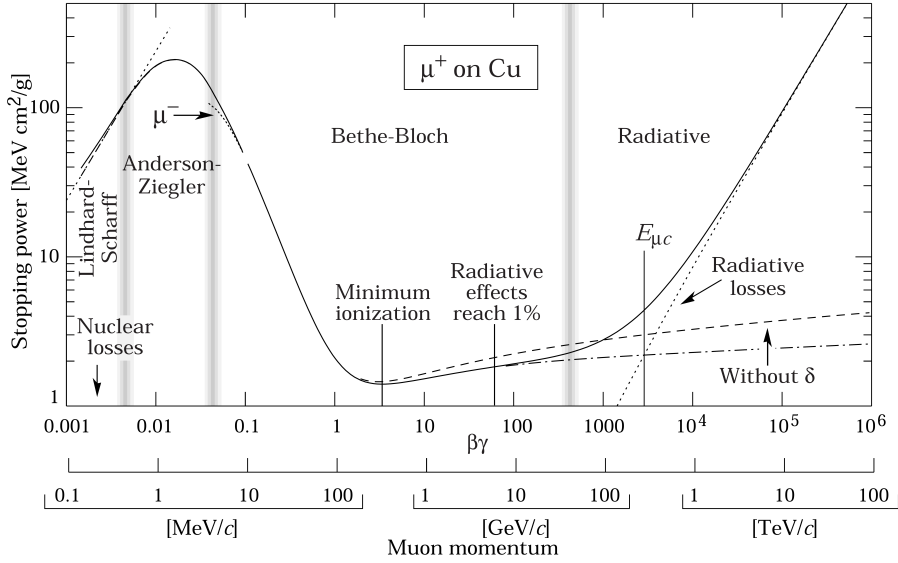


Figure 2.2: Energy loss of a muon in copper. The Bethe-Bloch formula (2.1) only describes a part of it [5].

thus with a mean excitation energy  $W = 3.6$  eV creating

$$n_{e/h} = \frac{\langle \Delta E \rangle}{W} = 24271 \quad (2.2)$$

electron/hole-pairs. These are mean values, but as the energy loss is described by the Landau distribution these are not the most probable values, which are lower than the mean value.

For high energetic electrons another effect called Bremsstrahlung dominates the energy loss. It can be simply calculated via

$$-\frac{dE}{dx} = \frac{E}{X_0}$$

with  $X_0$  being the radiation length, which is  $X_0 = 22$  for silicon [6]. Because  $\frac{dE}{dx} \propto m^{-2}$  for Bremsstrahlung, it only dominates for electrons, though high energy muons as they can occur at LHC are also dominated by this effect (see Fig. 2.3).

Photons can interact in three ways:

- photo effect
- Compton effect
- pair production

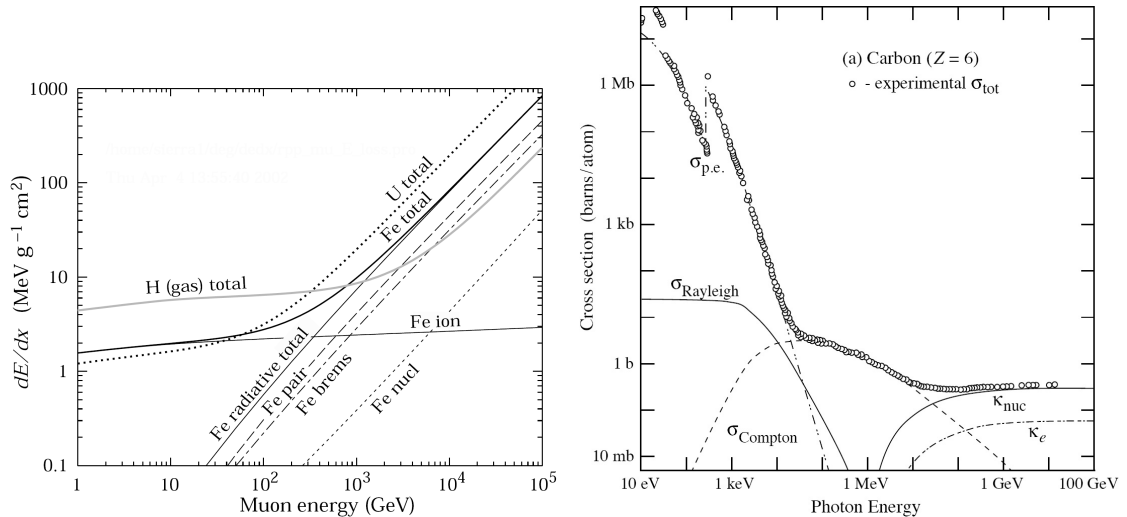


Figure 2.3: contributions to the energy loss of a muon (left) and different cross sections for a photon [5].

For a photon of typical energy only pair production is important when traversing the Pixel Detector. The whole energy will be deposited at once, thus it leaves only a single hit in one layer instead of one hit in each of the different layers.

### 2.1.2 Charge collection and noise

In order to collect the charge deposited in the detector material it has to be free of intrinsic charges. To achieve this, a pn-junction is used and then depleted. The voltage needed to deplete the whole sensor is proportional to its thickness squared [7]. If the detector is not fully depleted only the fraction of charge that was deposited in the depleted area can be collected. To decrease the drift time of the created electron hole pairs to the electrodes an additional external voltage is applied. This potential separates the electrons and the holes, as they are drifting to different electrodes. However, according to Ramo's theorem the induced charge on the two electrodes adds up. Ramo's theorem says [7]

$$i_k = -q\vec{v}E_Q \quad (2.3)$$

with  $i_k$  being the instantaneous current,  $q$  the charge,  $\vec{v}$  its velocity and  $E_Q$  the weighting field which depends on the geometry of the sensor. According to the theorem a charge is seen by the detector electronics as soon as it starts drifting to the electrodes but the full charge is only collected if the electron and the hole

reach the electrodes. Otherwise only a fraction of the signal would be induced in the electronics. This is the reason, besides being easy to segment and relativ radiation hard, that silicon is used as a detector material as it has a very long lifetime for free charges.

One has to note that not all charges will be collected by one pixel. Instead the electrons and holes are distributed over several pixels. A reason for this is thermal diffusion. The particles also do not always pass the detector vertical to the electrodes thus creating electron/hole-pairs over several pixels. Furthermore because of the external magnetic field the charge is not coercively collected in the pixel above which it was created. Unlike thermal diffusion this deflection is directed and can be calculated.

Most of the analysis in this thesis is based on noise from the detector. The noise contribution can be divided in three parts: noise from the sensor or amplifier and thermal noise. Thermal noise depends on the temperature and is always present, as well as noise from the amplifier, which scales with the frequency. If the sensor is depleted it contributes also noise, which depends on the leakage current [8]. To have a variable to characterise the noise the equivalent noise charge (ENC) is introduced. This is the amount of charge needed to simulate a signal which is equivalent to the noise.

## 2.2 The Pixel module

The modules consist of 250  $\mu\text{m}$  thick  $n$ -doped silicon, 16 front-end (FE) chips and one module-control chip (MCC). The silicon can be depleted by an external voltage up to 600 V [8], so that in the first years the sensor can be fully depleted. The pixel implants are connected via bump bonds (see Fig. 2.4) to a FE chip, which are organized in two rows. Although the FE chips were connected to the sensor with high precision, a small gap is still between them. The pixels which lie in this gap are either longer than normal pixels ( $50 \times 600 \mu\text{m}^2$  compared with  $50 \times 400 \mu\text{m}^2$ ) or ganged with pixels that are connected to a FE chip. So there is no blind spot on the module. A scheme of this can be seen in Fig. 2.4 on the left. All 16 FE chips are connected to the MCC, which is on the other side of the module and communicates with other on- and off-detector electronics.

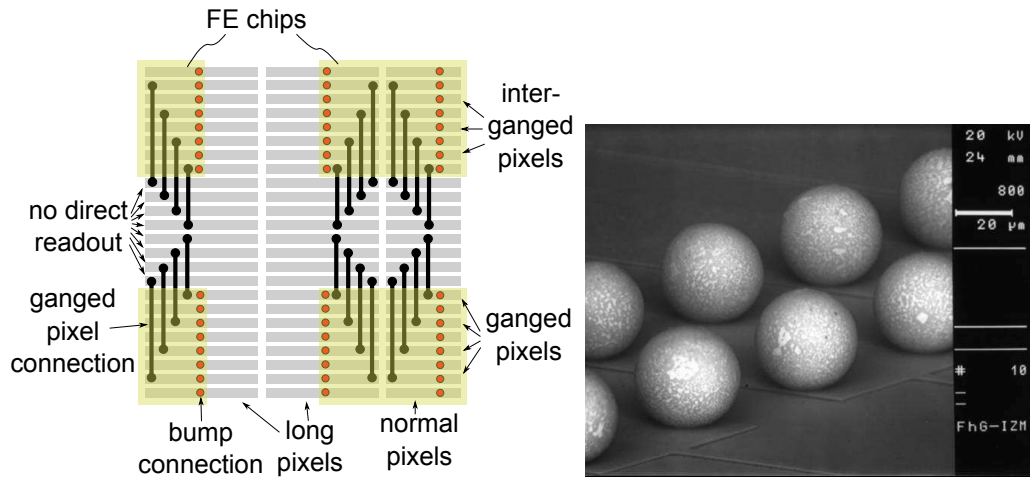


Figure 2.4: Left: scheme of pixels in the gap between the FE chips illustrating the different pixel types.

Right: lead-tin bump bonds [9].

### 2.2.1 The Front-End chip

Each FE chip is able to read out 2880 pixels. Because each pixel needs to be treated individually, it has its own read-out electronics. A scheme of the layout of one FE chip is illustrated in Fig. 2.5. As it can be seen the chip is divided in 18 columns with each 160 pixels with each pixel having its own analogue read-out. A circuit diagram of this part is illustrated in Fig. 2.6. It is connected to a pixel via a bump bond. The first part in the chain is a preamplifier. It has a capacitor which is discharged by a constant current. Because of this, the signal pulse after the preamplifier decreases linear, thus looking like a triangular, in contrast to an exponential behaviour when using a resistor instead of a capacitor. The amount of decrease is given by the constant current. The higher the current, the faster the decay. Thus the current can be set via a digital-analogue converter (DAC) either for the whole chip or for each pixel individually, called IF or FDAC respectively [10].

The final step in the analogue part is a discriminator. It gives out a binary one, as long as the signal is over its threshold, otherwise a binary zero. This is to separate a signal from a charged particle from normal noise. The typical value for the threshold is  $4000 e$  (as seen in Equation 2.2 the mean signal from a m.i.p. is  $\approx 25000 e$ ). It can be controlled with a global or individual DAC, GDAC or TDAC respectively, too. These values are tuned so that the time over threshold (ToT) of a signal from a m.i.p. is 30 bunch crossing units (BCU).

For testing purposes the analogue part has also charge injecting mechanism. There-

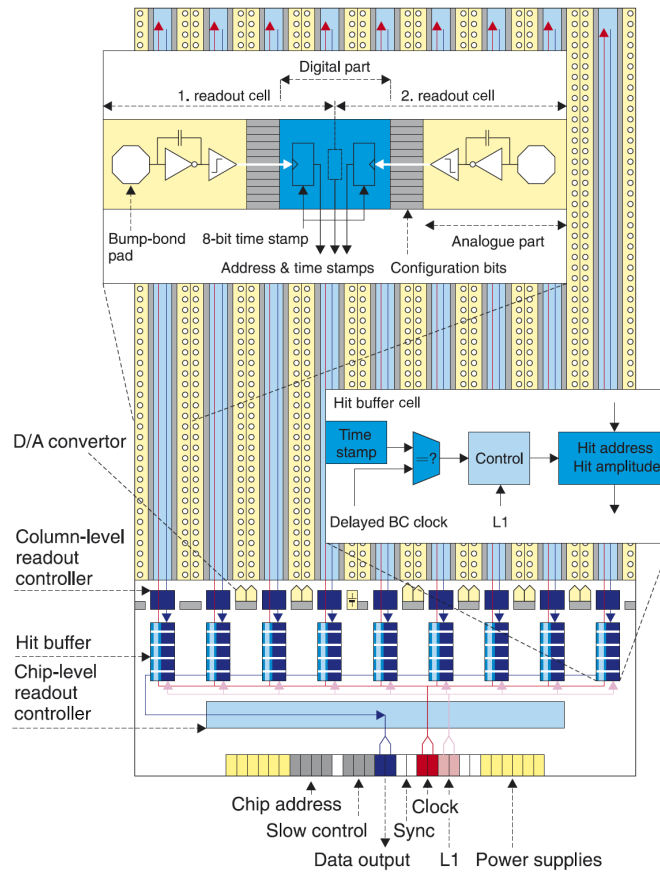


Figure 2.5: Scheme of the FE chip [10].

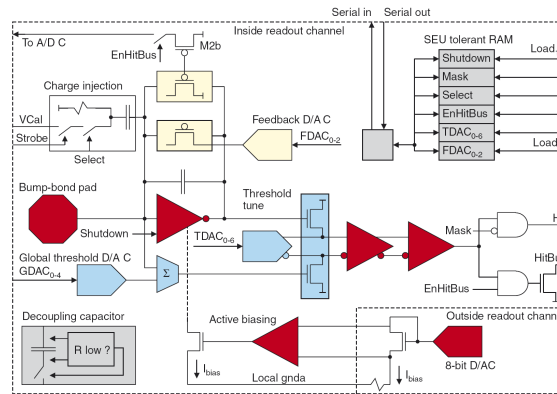


Figure 2.6: Scheme of the analogue part of the read-out. One for each of the pixel cells is available on the FE chip. [10]

for it has two capacitors  $C_{high}$  and  $C_{low}$  with approx. 40 fF and 7 fF respectively [8]. These can be charged and inject this charge in the preamplifier. Its value is controlled by a DAC called VCAL.

To store all the configuration data, i.e. the local DACs and other parameters like enabling read-out there are latches for each pixel.

The read-out of a pixel will not result in proceeding the signal from the discriminator but instead only proceed the time of the leading edge and the time difference to the falling edge of that signal. The time is given by a 7 bit counter. The ID of the pixel cell and the two times will be written in the read-out, if requested by the chip control. The chip control scans through every pixel in a column with a frequency of 40 MHz and checks if a pixel has detected a particle [9].

The digitisation of the charge pulse can cause a problem, when a second particle hits the sensor and the charge pulse of the first one is still over the threshold. In this case the charge pulses will add up and result in a long ToT, which seems to be caused by only one particle. But with an occupancy of  $5 \cdot 10^{-4}$  per normal pixel size, the probability of this to happen is fairly low considering a ToT of 30 BCU from a m.i.p. [8].

Every two columns share one read-out channel. It ends in the end-of-column (EoC) buffer. There are nine of them on the FE chip, one for each double column. The EoC only stores the data temporary and it is lost, if not read out. The read-out of it will only be done, if a trigger signal arrives and the time stamp of the leading edge matches the trigger plus a fixed latency.

For testing purposes it is better to read only specific pixel and not all at once, which would cause problems in the read-out channel. So often only every 32<sup>nd</sup> pixel is set to read out [8]. In order that the new configuration has not to be send to every pixel individually, when another pixel should be tested, it is possible to shift the configuration from one pixel to the next one.

### 2.2.2 Bump bond connections

The connection between the pixel inlays in the sensitivmaterial and the FE chip is established via bump bonds. These are small spheres either made of solder (PnSn) or indium depending on the place of production, IZM<sup>1</sup> or SELEX<sup>2</sup> respectively. Bump bonds are used because every pixel needs a connection to its analogue read-

---

<sup>1</sup>Intitut für Zuverlässigkeit und Mikrointegration, Berlin, Germany

<sup>2</sup>Sistemi Integrati, Roma, Italy

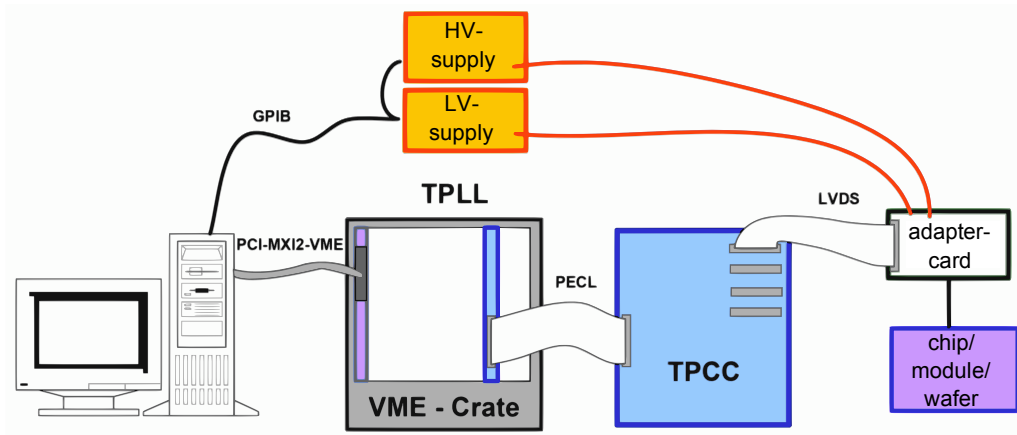


Figure 2.7: Setup for module testing called TurboDAQ [11].

out. Thus the density of connections is very high, making i.e. connections by wire impossible. The pitch between two bump bonds is about  $50\ \mu\text{m}$ , so the spheres which have a diameter of  $25\ \mu\text{m}$  need to be positioned precisely [8]. The final connection between the FE chip and the pixels is done by either heating the solder bumps or just using thermal-compression for indium bonds.

Besides defects of the FE chip, like scratches or electrical shorts, the bump bonds can be damaged, too. It can be that they are not connected to both the pixel and the FE chip, thus no connection is established. Over the production cycle it may happen that the number of those bonds increases due to mechanical stress. However, if detected early in the process there is a chance that they can be repaired. Another defect is the merging of two bonds. If a whole FE chip is defect it is possible to replace it with a new one.

### 2.2.3 Testing and production stages of the modules

To check the quality of the FE chips and modules, i.e. the bump bond connection quality or defects from radiation, they have to undergo several tests during production. The test setup is shown in Fig. 2.7. Via a VME interface the chips and modules can be configured and the injection mechanism can be controlled via a DAC. It is also possible to apply different voltages on the module and thus controlling the depletion depth. This is important for radiation strength tests, as when the sensor is not fully depleted less charge than possible is collected. The voltage needed to deplete the sensor increases with more radiation [9].

The first big series of tests after manufacturing the module is called ASSY. These

tests cover functionality tests as well as tuning of parameters, like a ToT of 30 BCU for a m.i.p.. For this thesis, an important test is the source scan, which means that the module is put under radiation of an radioactive source. The radioactive source is  $^{241}\text{Am}$  which emits photons with  $E \approx 60$  keV which translates into approx. 16,667 electrons in the detector, close to the signal a m.i.p. would give (see 2.2). The number of recorded hits for each pixel is stored. This test is very important, as disconnected or otherwise defect pixels can be detected in an easy way.

Another test is the measurement of the threshold which is usually adjusted to 4000  $e$ . In this test, a known charge is injected several times with different values and the number of signals over the threshold is stored. Ideally the probability for a hit should be a step function with the step at the value  $Q_{thresh}$  of the threshold. Due to noise in the sensor it is much smoother. The hit probability  $p_{hit}$  is given by [8]

$$p_{hit}(Q) = \Theta(Q - Q_{thresh}) \otimes \exp\left(-\frac{Q}{2\sigma_{noise}^2}\right) \quad (2.4)$$

with  $\Theta$  being the step function,  $Q$  the injected charge and  $\sigma_{noise}$  the ENC of the detector and amplifier. The threshold of the discriminator is the value at which half of the injected charges produce a hit. With this test it is also possible to measure the noise. This is done with and without depleted sensor.

The last important test is the ToT scan. With fixed threshold (normally to 4000  $e$ ), the ToT for different charges is measured several times.

After this initial testing the module is put under thermal cycling, the temperature is varied between  $-30$  °C and  $30$  °C, and long-term operation. The short test series after this is called BURN. The next series called FLEX is the main one. Unlike the series before, during this tests the module is cooled down to working temperature. As this is the last big test before mounting the modules on the support structures, all electronic tests are performed. It is so important because once the whole detector is installed in ATLAS it will not be accessible. As not all these tests are performed by one laboratory, the modules are shortly tested when arriving in a new lab. This series is called RECV. The next step in assembling the detector is, after thermal cycling, mounting the modules on the support structures, which are called staves in the barrel region. Thus the test after that is called STAVE and another short one directly before this step LOAD. The last regular test is called BIST and performed when the staves are merged to half shells. Since the staves are also send from one lab to another there is a short receiving test named STRC [12].

## 3 The ATLAS Trigger System

Every 25 ns a collision takes place at ATLAS. Due to the large number of particles produced in a single collision, an event can have a size of about 1.3 Mbyte when read out [1]. Thus it is technically and financially not possible to store all the data and only a fraction is read out. This is not a real problem, as most of the events cover no new or interesting physics. To determine the events that are worth to be progressed further a multi level trigger system is installed. A scheme of this is illustrated in Fig. 3.1. The first level uses data from the muon trigger chambers and the calorimeters. The muon trigger chambers are a tracking device, which can be read out very fast. But as a high accuracy for the muon momentum is required, there are other more precise detectors to determine the muon track. These, however, are not read out at this stage.

The level one trigger has 2.5  $\mu$ s to decide if an event is interesting, i.e. it has a high muon momentum or jet cluster in the calorimeter, or not. This reduces the event rate from originally 40 MHz to 75 kHz. If the event is interesting at this stage, the detector components including the Pixel detector are read out. When the read-out signal arrives later than 2.5  $\mu$ s after the event, the data of it will be lost. For the second level regions of interest derived from the first level are analysed. To achieve a fast decision just 2% of the total available amount of data is used. The process takes about 40 ms and reduces the rate to approx. 3.5 kHz.

Within the last trigger level, the so called event filter, all data passed level 2 is put together to build an event. Other than the first two levels, this trigger stage is located outside of the detector. The last filter has an output rate of approx. 200 Hz.

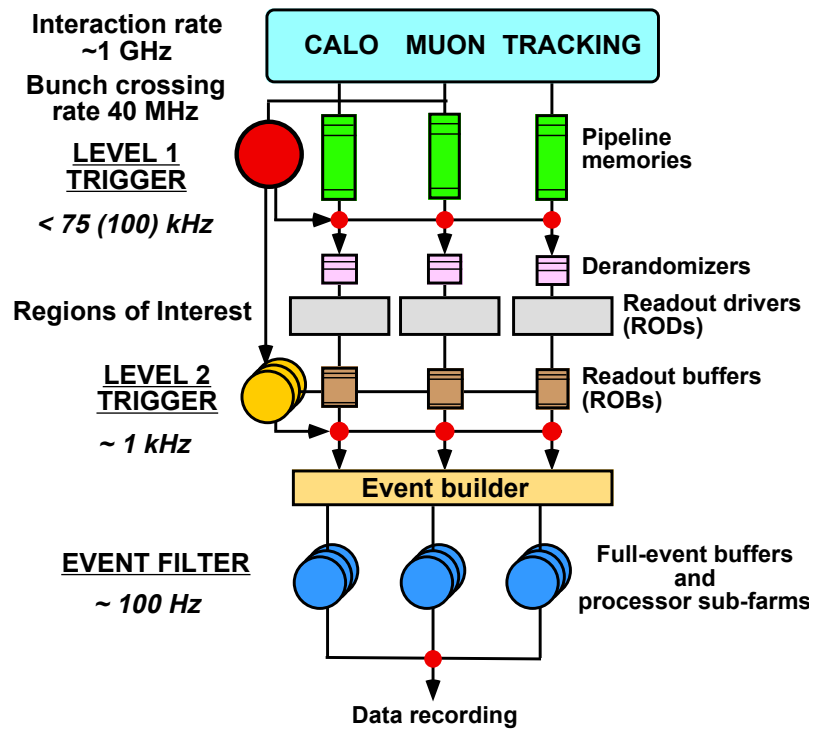


Figure 3.1: Levels of the ATLAS trigger [13].

# 4 Analysis of bump bond connection quality

As stated earlier, the bump bonds connect the analogue read-out part to the pixel. If this connection is not done correctly the whole pixel will be dead and not record a hit. Hence for the full analysis of an event it is important to know those dead pixels.

The easiest way to detect dead pixels is a source scan, as already mentioned in chapter 2.2.3. During this test the module will be put under irradiation of a radioactive source. This test, however, is not available once the modules are put in the detector. As the amount of dead pixel might change over time it is important to find an alternative method like noise from threshold scan (see chapter 4.1.2) to detect them.

## 4.1 Module tests

### 4.1.1 Source scan

An  $^{241}\text{Am}$  source is used to put the modules under irradiation. The expected result is that every pixel should obtain the same amount of hits. For this to happen it is important that the pixels are calibrated in the same way and the sensor is depleted. That is why this test is done after threshold and ToT tuning. As the MCC is facing the radioactive source there are eventually some pixels which will report less hits than others because of the structure of the MCC, like conductors, which shields the pixel below it. But these pixels, when connected right, should record hits nevertheless although at a lower rate. If a bump bond is unconnected the pixel should show not a single hit. The source scan is, however, not a good method to detect merged bump bonds. In this case one pixel would show hits and the other not, as one of the analogue parts has a slightly higher potential and so

collects all charge from the detector. But the one which shows hits should report about the twice the number than normal as it practically reads out two pixels. This amount has to be seen in relation to pixels of the same type, i.e. long ones as they should initially detect more than a normal one.

### 4.1.2 Noise from threshold scan

In a threshold scan the value of a fixed threshold is measured for each pixel. This is done by injecting a known charge via the injecting circuit several times and report the response of the discriminator. After several injections, VCAL is increased one step and so is the charge. Ideally, the response would be a step function with the step at the value of the threshold. This, however, is not the case. Through the noise in the amplifier-detector system it is more smooth, as a charge normally under the threshold can pass the discriminator if the noise is high enough. This can be described with Equation (2.4).

The amount of that noise can give an indication if a pixel is connected to its read-out part. The scan is done with and without depleted sensor. One would expect that the noise from an unconnected pixel is significantly lower than from connected ones, as the sensor itself causes some noise. Another effect should be that the noise difference between a depleted and an undepleted sensor for unconnected pixel is close to zero instead of several  $100 e$  for connected ones [8].

So this should be a method to determine if a bump bond connects the pixel to its read-out correctly or not. As the threshold scans do not need any outside preparations, it can be done even with the modules already installed in the detector.

## 4.2 Computational analysis of test data

For the analysis, production test data of 1852 modules from the stages ASSY, BURN, FLEX, STAVE and BIST were available. However, not for every module every stage had data. As only at the stages ASSY, FLEX and STAVE all three tests that give information about the quality of the bump bonds were performed, the analysis only focuses on these three stages.

The algorithm was written in ROOT and loops over every module of the stage that is analysed. The aim for this run is to find correlations between dead pixels from source scan and the amount of noise with depleted sensor or the noise difference

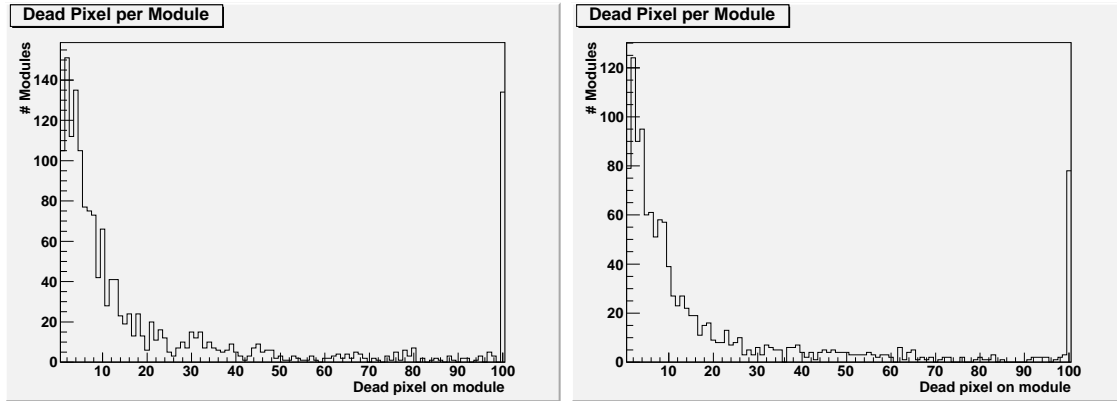


Figure 4.1: Distribution of dead pixels per module for ASSY (left) and FLEX (right). Note that all modules with more than 100 dead pixels are combined in bin 100 (overflow bin).

between depleted and undepleted sensor. The first step is to extract the amount of hits reported during a source scan. Every pixel which has not a minimum amount of hits is labeled dead. Unless stated otherwise, the minimum number of hits is one. During the next step the noise of each pixel with and without depleted sensor is determined. This had not to be calculated via Equation (2.4), but is instead already stored in the given data. All this data is histogrammed and split up in the pixel types, i.e. long pixels, and the material used for the bump bonds. The last step of the analysis is the calculation of the correlation between the parameter from source and threshold scan.

It is also interesting to know how the amount of dead pixel changes during production. So a similar algorithm is used, which loops over ASSY and FLEX. The correlation of noise from the depleted sensor between the two stages is analysed.

## 4.3 Results

### 4.3.1 Results from the source scan

The distribution of dead pixels, that were identified via a source scan, per module for ASSY and FLEX is shown in Fig. 4.1. It can be seen that at ASSY stage many more modules have a higher number of dead pixels than at FLEX stage with mean values of  $\mu_{ASSY,all} = 37.08$  compared to  $\mu_{FLEX,all} = 30.79$ . One reason for this is that some modules with many dead pixels have no FLEX data or data from later stages and so may be discarded. So it is reasonable to analyse modules with ASSY,

#### 4 Analysis of bump bond connection quality

	normal	long	ganged	inter-ganged	long ganged	long inter-ganged
ASSY	0.035%	0.223%	0.173%	0.061%	0.516%	0.359%
FLEX	0.035%	0.194%	0.173%	0.055%	0.539%	0.343%
STAVE	0.040%	0.369%	0.212%	0.056%	0.737%	0.478%

Table 4.1: Probability of a dead pixel for the different types at various production stages.

FLEX and STAVE data, which will be done from now on, if not stated otherwise. This leaves 1096 modules for analysis. The mean values of dead pixels per module are:

$$\begin{aligned}\mu_{ASSY} &= 27.85 \\ \mu_{FLEX} &= 26.46 \\ \mu_{STAVE} &= 37.80\end{aligned}$$

The probabilities of a defect in the different pixel types are given in Tab. 4.1. It can be seen that the long pixels have five to ten times the probability of being defect as normal pixels. This is probably due to mechanical stress as the long pixels are located at the edge of the FE chip. Thus they are more vulnerable to tension than normal pixels. This tension can occur during transport between the labs, when mounting the modules on the support structures or due to thermal cycling. The same argument holds true for the ganged and inter-ganged pixel, which have both higher percentage of defects than normal ones, but not as high as long ones. This is probably because these two groups of pixels are not all direct at the edge of the FE chip. However, the long ones from these groups have the highest failure rates. This seems logical, because these are pixels directly located at the corner of the FE chip. As expected, the ratios of dead pixels for modules with data from the three stages are much lower than the ratios for all modules at that stage. Notable from ASSY to FLEX stage is the decrease of dead long pixels. Some defect bump bonds for these pixels could be fixed, as these are easier to access than other pixels. All other percentages stayed roughly the same. In contrast there is a huge increase from FLEX to STAVE by over ten dead pixels per module. Especially the dead long pixels have increased drastically. This is probably mainly due to mechanical stress, as the modules were mounted on the support structures.

In Fig. 4.2 all dead pixels from the 1096 modules are projected on one FE chip, so

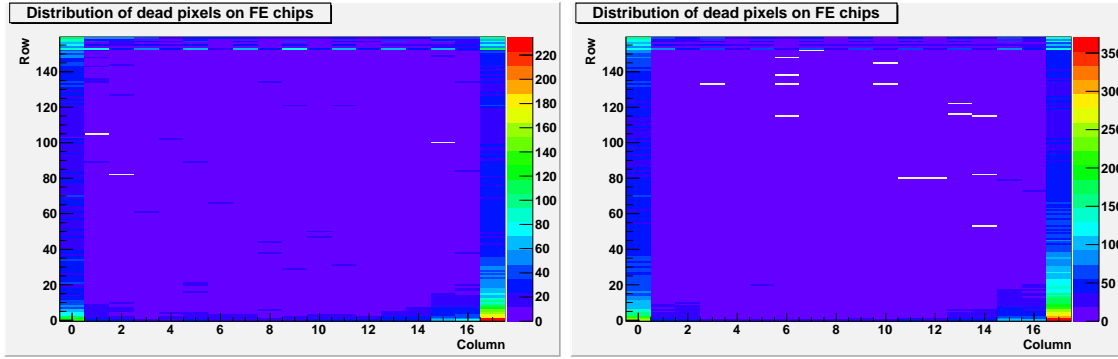


Figure 4.2: Distribution of dead pixels over the FE chip at FLEX (left) and STAVE (right) stage. All dead pixels are projected on one FE chip. The columns to the left and right represent long pixels. The ganged and inter-ganged pixels can be found at the top.

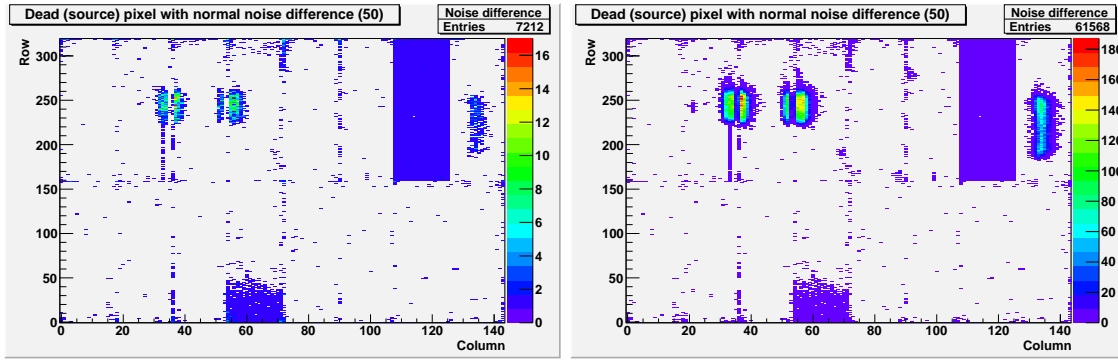


Figure 4.3: Pixels from all analysed modules that show not enough hits in the source scan at FLEX stage, but have a normal noise difference of more than  $50 e$  between a depleted and an undepleted sensor. The number of minimum hits is five (left) and ten (right).

that the distribution of dead pixels over the FE chip can be seen. It is noticeable that dead pixels are likely to be found on the edges of the FE chip, especially in the corners. That this number increases sharply from FLEX to STAVE stage, proves the assumption that most defects are caused by mechanical stress. Besides others, the innermost ganged pixels have a pretty high failure rate compared to other ganged pixels, especially at FLEX stage. However, they also have a pattern that is especially true for every second column, which can not be explained so far.

For the analysis above it was assumed that a pixel reporting at least one hit is not dead. This minimum is chosen manually. However, as illustrated in Fig. 4.3 it should not be put too high, because more and more working pixels will be labeled dead. When compared to the left histogram in Fig. 4.4 an increase of dead pixels can

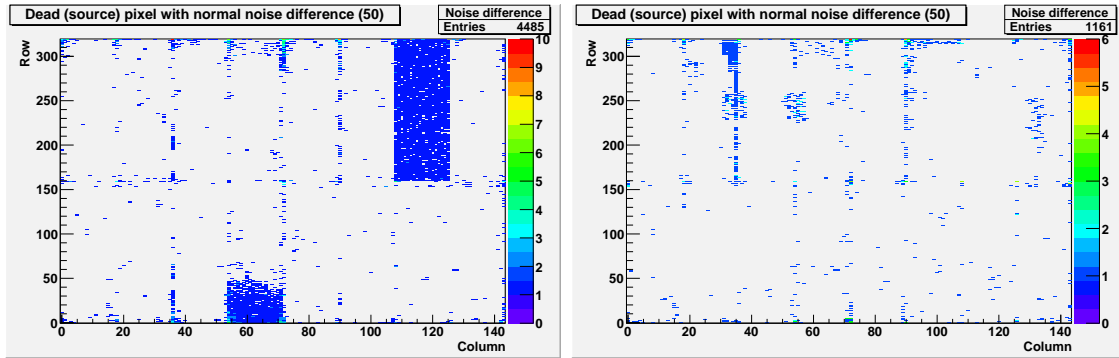


Figure 4.4: Same histogram as in Fig. 4.3 but the number of minimum hits is only one. On the left at FLEX and on the right at STAVE stage.

be seen at three locations. These pixels lie under a capacitor or another structure of the MCC and are slightly shielded from the radiation. However, there seems to be some pixels at FLEX stage that show a normal noise difference but no hits in the source scan, namely one and a half modules. As these pixels do not occur at STAVE stage (on the right in Fig. 4.4) it is assumed that these pixels were masked out at the source scan at FLEX stage, which was not especially indicated in the source scan files. This effect is only seen at FLEX stage and so might cause some problems during further analysis because one module with wrongly labeled normal pixels would contribute around one sixth of all dead normal pixels detected at source scan. At STAVE stage, however, the three locations of pixels shielded from the structure are slightly visible. An appropriate solution for this is a short time of radiation exposure.

As the noise from the amplifier is far below the threshold of 4000  $e$ , it can not cause reported hits. So it is no problem to choose the minimum number of hits as one.

### 4.3.2 Results from the threshold scan with depleted sensor

The noise from a depleted sensor is expected to be generally lower than from an undepleted. Nevertheless there should be a difference in noise if the bump bond connects the sensor or not. The estimated noise for an unconnected normal pixel is 120  $e$  instead of 160  $e$  for a connected one [8]. The noise distribution for all pixels is shown in Fig. 4.5. The expected peak is clearly visible although it is slightly shifted to higher noise of approx. 190  $e$ . The long tail to higher noise values and the second small peak is mainly caused by the long pixel.

The goal in this part of the analysis is to find a value of noise for which can be

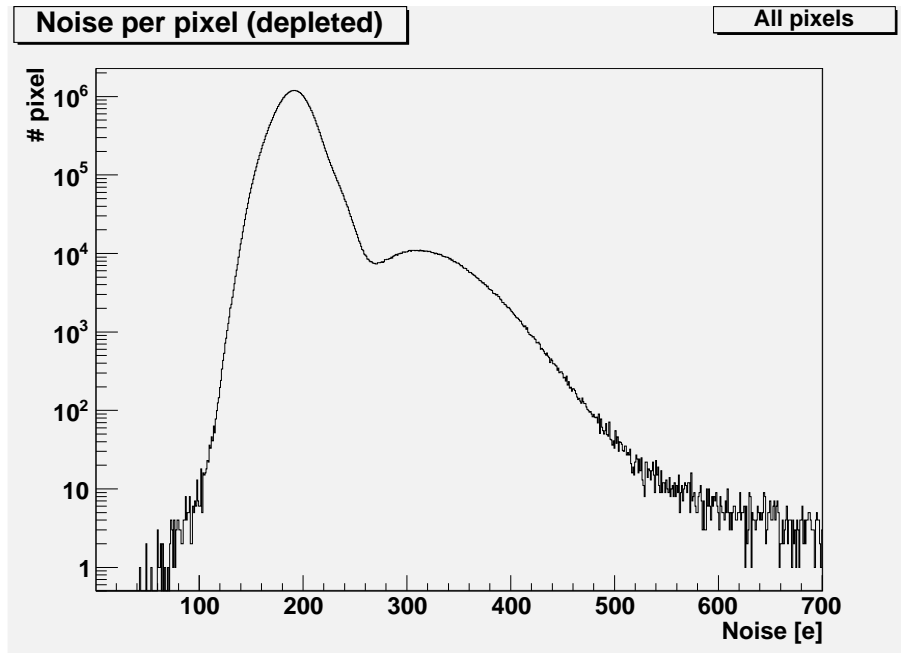


Figure 4.5: Number of pixels with a specific noise with depleted sensor for all analysed pixel at STAVE stage.

assumed, that most pixels with lower noise are dead and only a few dead pixels have a higher noise. The problem of this is illustrated in Fig. 4.6, where the noise from pixels labeled in the source scan as dead or working respectively is plotted. As it can be seen, the noise from dead pixels is separated from the noise from working pixels with a slightly overlap. The peak for noise from dead pixels is at approx. 140 e, which is a little higher than expected but should do no harm as the peak of noise from working pixels at 190 e is also slightly shifted to higher noise. The overlap at low noise should cause no big problems, but the overlap at noise higher than 165 e can not be ignored as there are still numerous dead pixels with noise above this. It should be noted, that pixels with zero noise are excluded from these graphs.

To evaluate the performance of discriminating the dead pixels three ratios are calculated. They are defined as

$$R_d(\text{noise}) = \frac{\text{number of dead pixels with less or equal } \textit{noise}}{\text{total number of dead pixels}}$$

$$R_a(\text{noise}) = \frac{\text{number of pixels with less or equal } \textit{noise}}{\text{total number of pixels}}$$

$$R_w(\text{noise}) = \frac{\text{number of dead pixels with less or equal } \textit{noise}}{\text{number of working pixels with less or equal } \textit{noise}}$$

#### 4 Analysis of bump bond connection quality

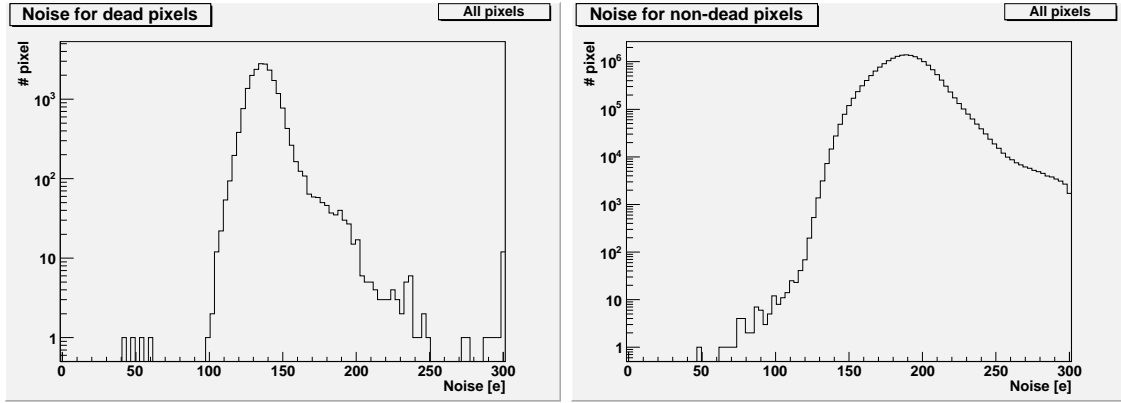


Figure 4.6: Noise from dead (left) and from non-dead pixel (right) at STAVE stage for all pixel types combined. The pixels were grouped according to their results in the source scan. Note that the last bin for dead pixels shows the overflow.

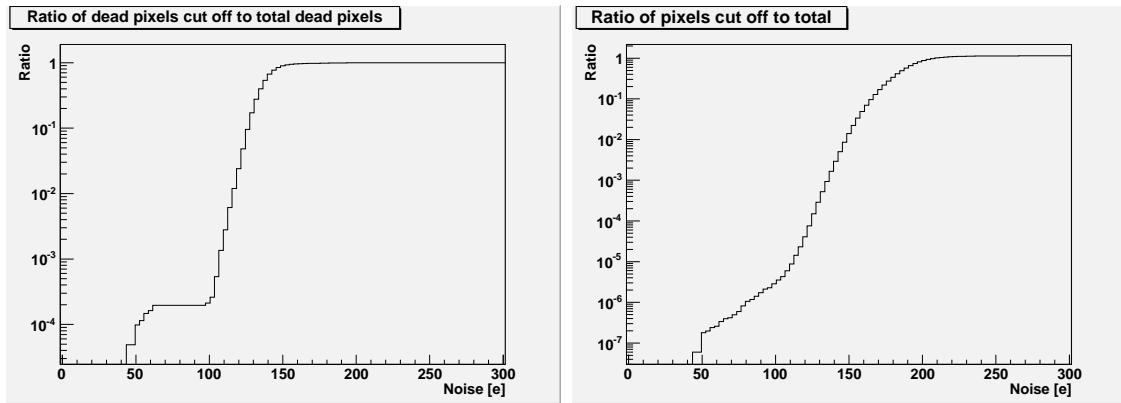


Figure 4.7: Ratios  $R_d$  (left) and  $R_a$  (right) for all pixels at STAVE stage.

The ratio  $R_d$  is shown in Fig. 4.7 on the left and the ratio  $R_a$  on the right. A minimum noise of 144  $e$  would discard 79.95% of the dead pixels and a little more than 0.5% of all pixels. For every disabled dead pixel, around five working pixels would be disabled. Further increase of the minimum has to be done carefully as a threshold of 147  $e$  would switch-off 86.67% of the dead pixels but also around 1% of all pixels.

To further increase the performance the minimum noise is not set as one value for all pixels, but differently for every pixel type. As the noise depends to some extent on the size of a pixel this is reasonable. The ratios for a threshold which discriminate at least 80% of dead pixels for the different pixel types is given in Tab. 4.2. Especially for long and long inter-ganged pixels dead pixels are effectively discriminated. So

pixel type	threshold [e]	$R_a$ [%]	$R_w$ [%]
all	145	0.72	0.16
normal	143	0.43	0.07
long	143	0.65	14.02
ganged	184	1.39	0.10
inter-ganged	165	2.31	0.02
long ganged	179	5.29	0.60
long inter-ganged	159	0.94	3.05

Table 4.2: Ratios and threshold for disabling at least 80% of the dead pixels (STAVE).

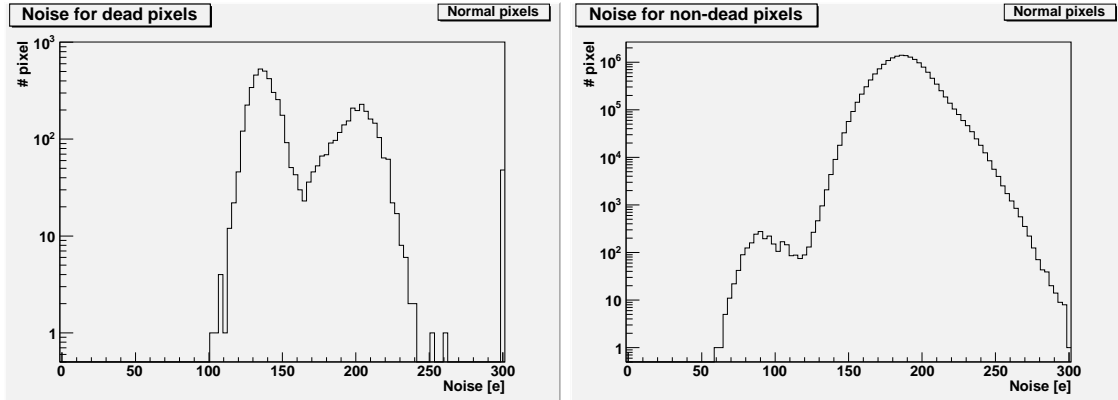


Figure 4.8: Noise from dead (left) and from non-dead pixels (right) at FLEX stage for normal pixels. Note that the last bin for dead pixels shows the overflow.

the performance could be further increased setting  $R_d$  individually for each type. With the different thresholds 0.52% of all pixels are discriminated, when 80% of dead pixels for each pixel type are discarded, compared to 0.72% with one threshold for all pixels.

While these results apply for modules at ASSY stage too, modules at FLEX stage are different. The ratios at this stage are much worse than at the other two. The main reason for this is bad ratios for normal pixels that are illustrated in Fig. 4.8. The noise from dead and working pixels is not separated any more, so that a good threshold is difficult to find. To discriminate 50% of the dead pixels 10% of all normal pixels are turned off, which is an unacceptable result. The reason for this is probably the wrong labeled dead pixels from the source scan that can be seen in Fig. 4.4 on the left. What proofs this point is the fact that the ratios for other pixel types are only slightly off and that the noise from dead pixels has a second peak at

Stage	ASSY	FLEX	STAVE
$R_{IZM}$ [%]	26.07	26.64	25.16

Table 4.3: Ratio  $R_{IZM}$  for dead pixels of modules with lead-tin bump bonds showing noise.

the main peak of the working ones. For unknown reasons the noise from non-dead pixels has also a small peak around 90  $e$ . As the normal pixels have a very low failure rate the wrong labeling has a strong impact. Because 85% of all pixels are normal ones the ratios if set for all types the same, are worse, too.

### 4.3.3 Results from the threshold scan with undepleted sensor

With an undepleted sensor the noise from the amplifier-sensor system should be higher than from a depleted sensor due to the undepleted sensor working as a capacity. However, for this analysis it is needed to differentiate between the two bump types lead-tin and indium respectively.

Lead-tin has a very low resistance and as the pixels are effectively shorted with an undepleted sensor an injected charge should not be detected at the discriminator [8]. So if a bump bond is not connected to the sensor an injected charge should be recognized at the discriminator and thus the pixel should have noise. In fact this is only true for around every fourth unconnected pixel (see Tab. 4.3). So this is not a very reliable method for disabling defect bump bonds.

Indium on the other hand has a large resistance, so that the shortening of the pixels has no noticeable effect. However, there should be a significant increase of the noise compared to a depleted sensor due to the capacity if the bump bond is connected to the sensor. If not, the noise should be equal or with little difference to the noise from a depleted sensor. This is why the noise difference for these modules is analysed.

The spectrum of noise difference is shown in Fig. 4.9. Besides a main peak at approx. 250  $e$  and a long tail to higher differences, a small peak around zero is noticeable. This should be the dead pixels. The noise difference for dead and working pixels is mapped in Fig. 4.10. Around zero a peak for the noise difference from dead pixels is clearly visible. The spectrum has two clearly visible exponential contributions. The bigger one is probably caused by normal sized pixels and the other from long pixels. The noise spectrum of working pixels peak around 250  $e$ .

Again the ratios  $R_d$ ,  $R_a$  and  $R_w$  are calculated. In Fig. 4.11  $R_d$  and  $R_a$  can be seen.

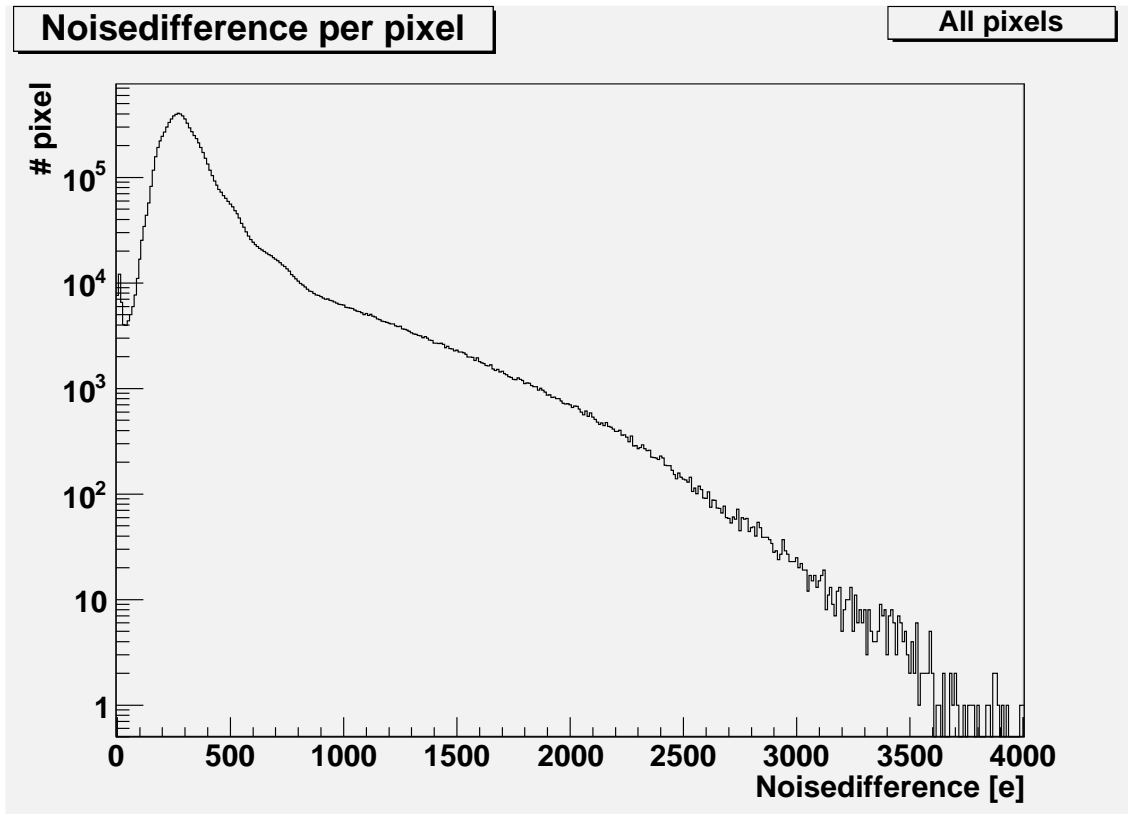


Figure 4.9: Spectrum of noise difference for modules with indium bump bonds. Note the absolute value is plotted.

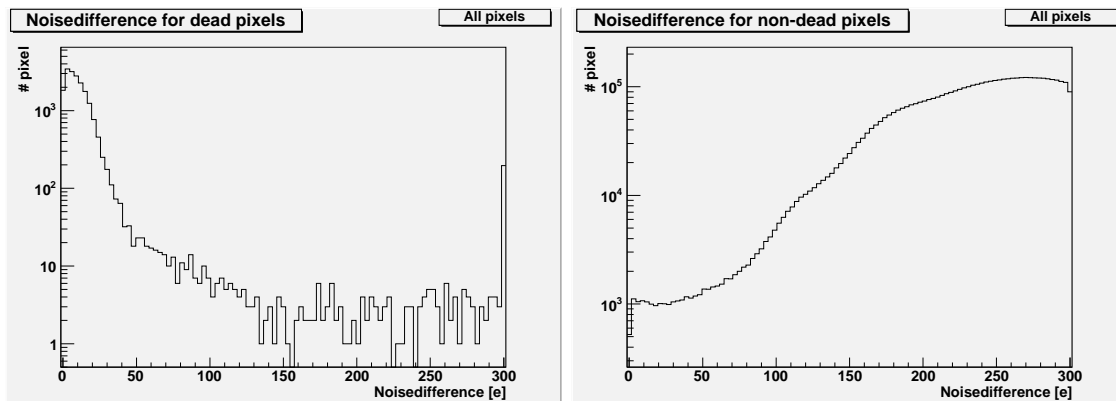
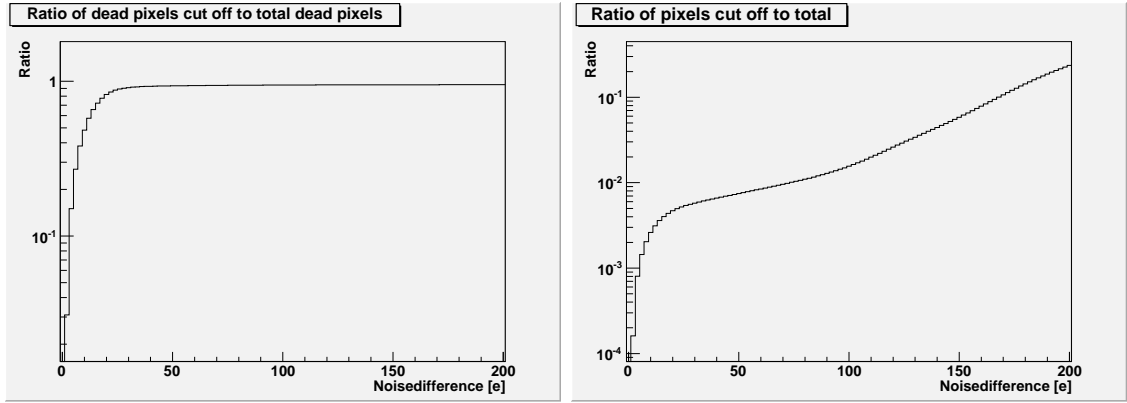


Figure 4.10: Noise from dead (left) and from non-dead pixel (right) at STAVE stage for all pixel types combined. The pixels were grouped according to their results in the source scan. Note that the last bin for dead pixels shows the overflow and that the absolute value is plotted.

Figure 4.11: Ratios  $R_d$  (left) and  $R_a$  (right) for all pixels at STAVE stage.

pixel type	threshold [e]	$R_a$ [%]	$R_w$ [%]
all	18	0.46	2.48
normal	18	0.18	1.17
long	17	3.04	4.72
ganged	36	0.47	0.43
inter-ganged	21	0.10	9.27
long ganged	40	6.02	0.54
long inter-ganged	23	2.49	2.62

Table 4.4: Ratios and threshold for disabling at least 80% of the dead pixels (STAVE).

Compared to the same ratios with depleted sensors  $R_d$  reaches 100% relative soon in relation to  $R_a$ . As the noise with depleted sensor depends on the pixel type, the noise difference should do so, too.

The results for  $R_d \geq 80\%$  for a fixed threshold for all pixels and for an individual one for each type are given in Tab. 4.4. What is notable, is that for normal, ganged and inter-ganged pixels, this method for the chosen  $R_d$  is more effective than the method with depleted sensors, while for the others it is vice versa. What kind of method should be used depends on the pixel type.

The results from FLEX stage are again significantly different, probably again due to wrong labeling.

#### 4.3.4 Combined results

The next step is to combine the two methods described above. To do this the correlation between the noise from depleted sensors and the noise difference is mapped

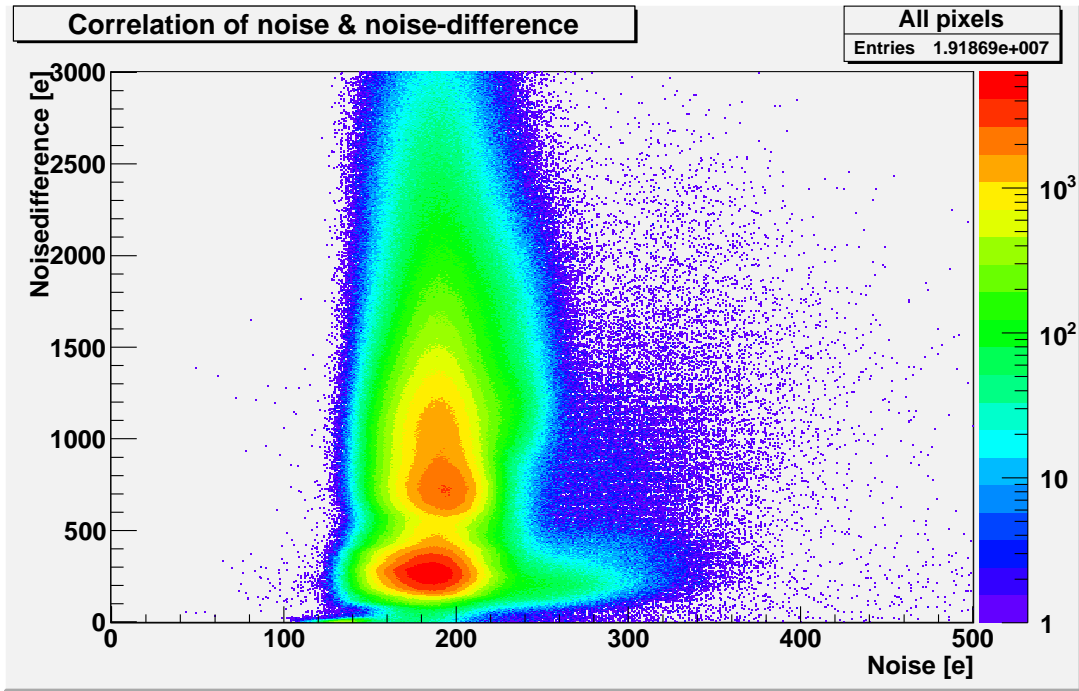


Figure 4.12: Correlation between the noise from depleted sensors and the noise difference for all pixels at STAVE stage.

in Fig. 4.12. There are two visible peaks, which come from the different pixel types, but really interesting for this analysis is only the lower left corner. This is where the dead pixels should be. Their correlation is illustrated in Fig. 4.13. Compared to the correlation for non-dead pixels, which is plotted in Fig. 4.14, they are separated. So combining the two methods would probably increase the accuracy of detecting dead pixels.

FLEX again has some issues. As can be seen in Fig. 4.15 the correlation of noise and noise difference for dead pixels is for most in the expected area, but for some in the area of the main peak for normal working pixels. These are probably the wrongly labeled ones. A third small group of dead pixels show the expected low noise, but no correlation of the noise difference at all. This group is also visible at STAVE stage (see Fig. 4.13), whereas the dead pixels with normal correlation of noise and noise difference are only observed at FLEX stage. This gives further evidence, that these pixels were labeled wrongly.

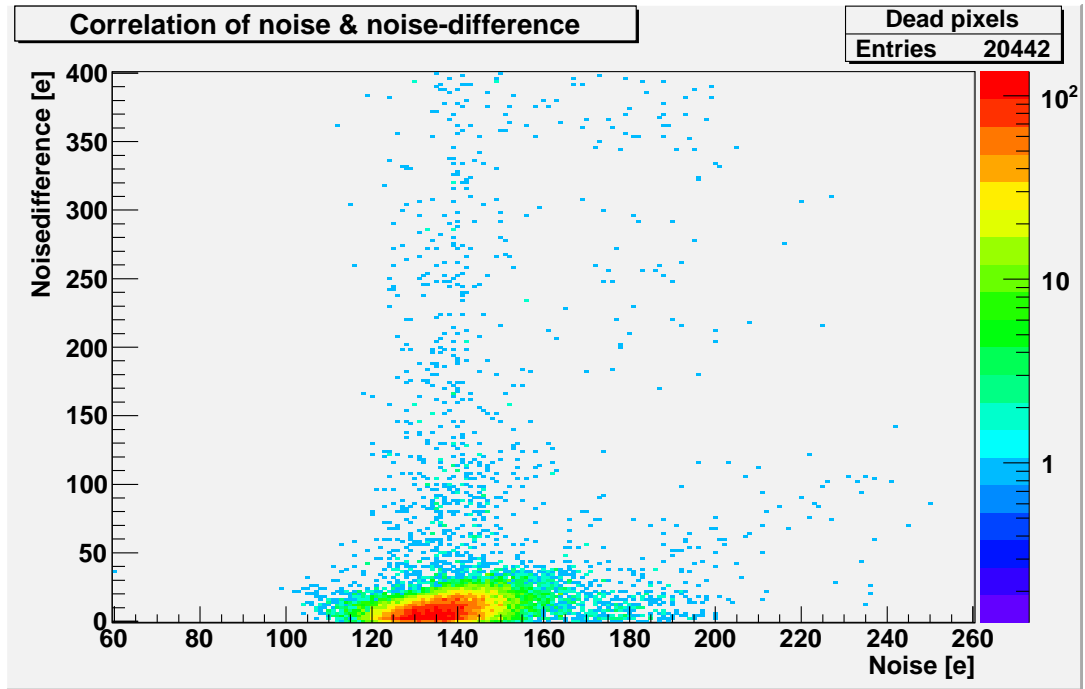


Figure 4.13: Correlation between noise from depleted sensors and noise difference for dead pixels at STAVE stage. Few dead pixels with high noise difference are cut off.

#### 4.3.5 Correlation between ASSY and FLEX

In Fig. 4.16 the correlation of the noise from pixels with depleted sensors between ASSY and FLEX stage is illustrated. It can be seen that the noise of most pixels correlates at both stages. The pixels which got damaged between the stages are visible as a accumulation under the main correlation area.

### 4.4 Merged bump bonds

To find merged pixels via a higher than expected hit rate in the source scan is not trivial. As some structures shield the pixels from radiation the hit probability differs not only for the different pixel types but also within these groups. So the hit rate of a pixel has to be compared with pixels from other modules at the same position. Here is the problem, that not every module might have had the same amount of radiation in the source scan and so the number of hits a pixel should detect may vary from module to module.

However, merged pixels should also have a dead pixel as neighbour. This dead

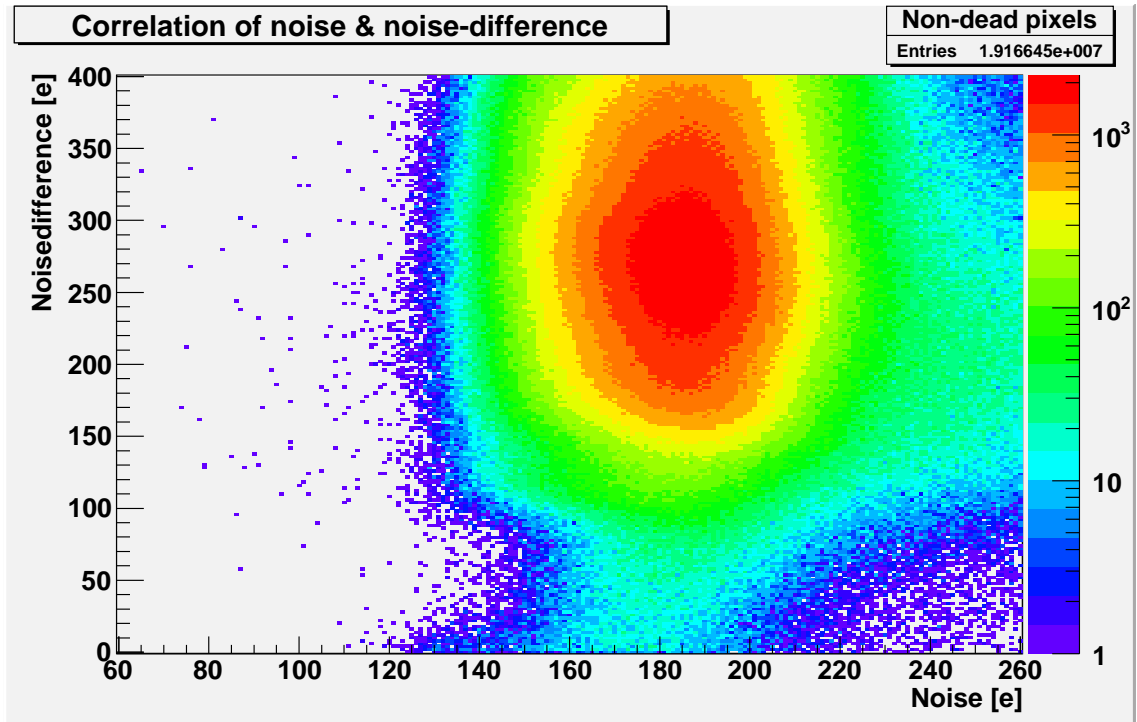


Figure 4.14: Correlation between noise from depleted sensors and noise difference for working pixels at STAVE stage.

neighbour should be in the same column, as here the pixels are only separated by  $50 \mu\text{m}$ . Additionally to a higher hit probability, the merged pixels should also have a higher noise with depleted sensor. An algorithm that searches for those pixels with a noise higher than  $250 e$  and a dead neighbour detects 430 potentially merged pixels. This number seems a little low, so either the probability of merged pixels is pretty low or not all were detected with this algorithm.

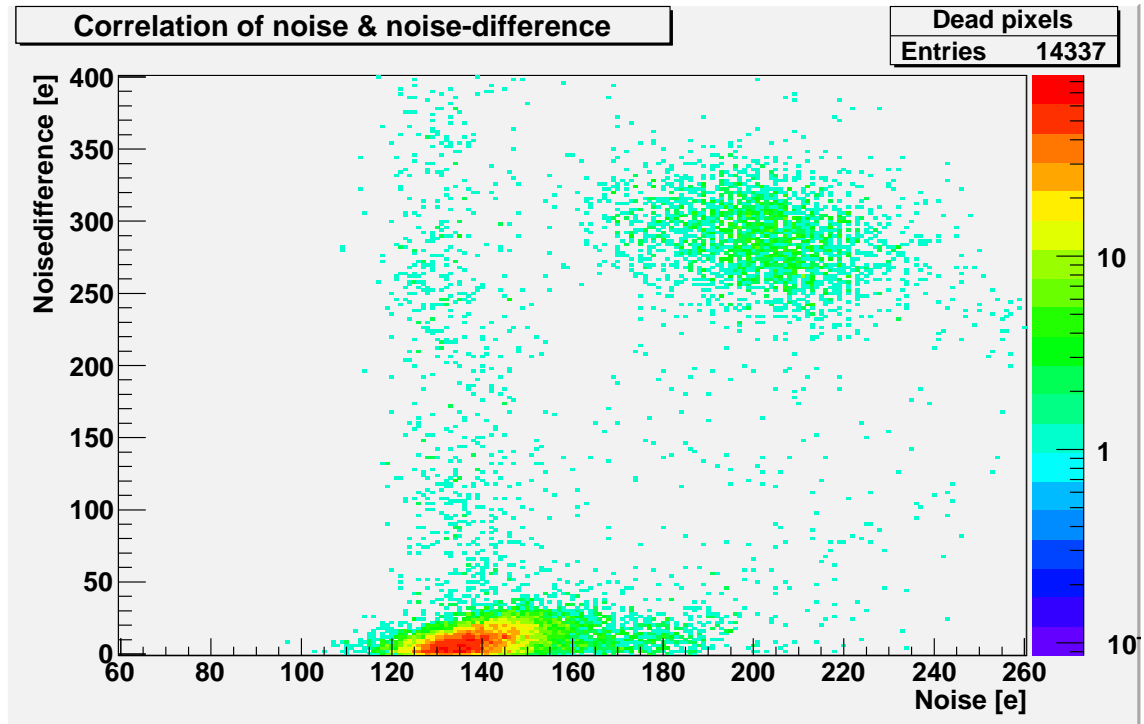


Figure 4.15: Correlation between noise from depleted sensor and noise difference for dead pixels at FLEX stage.

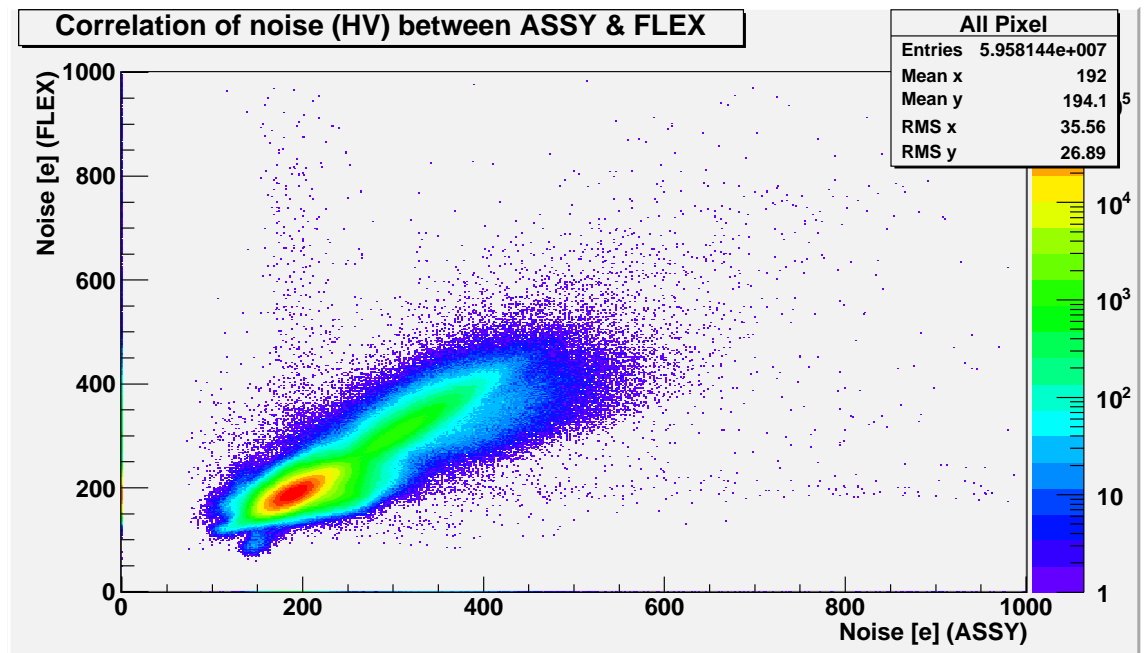


Figure 4.16: Correlation for noise from depleted sensor between ASSY and FLEX.

## 5 Time over threshold analysis

The aim of this analysis is to find a good function which describes the relation between ToT and detected charge as accurately as possible.

Each particle detected in the sensor causes a charge pulse. As seen in Chapter 2.1.1 this charge is characteristic to each particle and is therefore, together with time information of the hit, read out of the detector. The charge pulse is an analogue signal and thus hard to propagate in electronics. The solution is to digitise the charge pulse. As the configuration of the current of a pixel and the voltage of the sensor stays the same for every hit, the ratio of the height of the charge pulse to the total amount of deposited charge stays constant. So it is enough to read out the height of the pulse to gain all information, as long as the height is calibrated to the charge.

There are two ways to digitise the pulse height. The first is to use several discriminators with different thresholds. Each discriminator with a threshold lower than the pulse height will respond, each with a higher one will not. The charge resolution is thus given by the interval between two thresholds. To tune the resolution more discriminators have to be used, which is a major drawback when considering that this has to be done for each pixel on a space of roughly  $50 \times 400 \mu\text{m}^2$ . The advantage would be that the height of the charge pulse is known instantly.

The other method is used in the Pixel Detector and requires only one discriminator with a certain threshold. Here the pulse height is not measured directly but only its time over threshold (ToT). The connection between those two is illustrated in Fig. 5.1. As the capacitor above the amplifier (see Fig. 2.6) is discharged by a current source, the falling edge of the signal can be assumed to be linear and thus the charge pulse as a triangle. This is not entirely correct because the edges of the triangle are not as sharp as in the picture but more smooth. This effect is considered small and neglected. Thus the height of the pulse is directly proportional to the time the falling edge needs to reach zero. However, the ToT has also a contribution from the leading edge. For the leading edge it takes a fixed amount of time to reach the maximum.

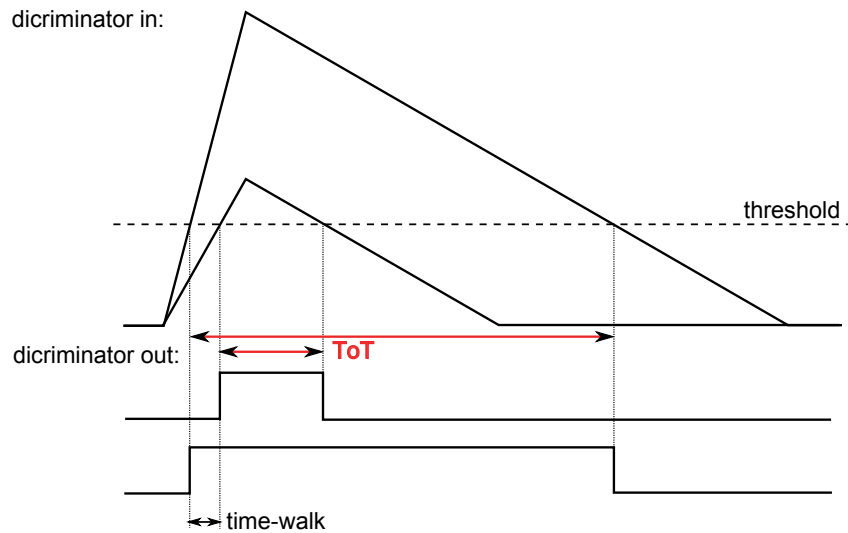


Figure 5.1: Scheme for the relation between the charge pulse and ToT for two different charges.

This time is independent from the charge. The contribution to ToT certainly is not. The time difference for two charges with aligned first rising to reach the threshold is called time-walk. In order to minimize this effect the amplifier should be as strong as possible giving of extra heat and power consumption. The advantage of this method to digitise the charge is that only one discriminator is needed. The disadvantage is the long time till the end of the ToT is reached and the non linear connection of ToT to pulse height because of the time-walk. At the Pixel Detector the discriminator output is monitored every 25 ns, a so called bunch crossing unit (BCU). One BCU is needed for the leading edge to reach the maximum. The current source is calibrated such that the signal of a m.i.p. gives a ToT of 30 BCU. This is due to the fact, that the deposited charge is often distributed over several pixels and that the function used at the moment to describe the relation between ToT and charge fits not well for low ToT (see 5.2). The threshold has a nominal value of 4000  $e$ .

To find a good function which describes the relation between ToT and pulse height, different functions are fitted on ToT data for different charges. This is either be done for each pixel or for the whole FE chip. The motivation is that a linear function does not describe the connection very well and the currently used function has no physical motivation. It is nice to know if the fit parameters have to be stored for every single pixel or if it is acceptable to store only one set of parameters for each FE chip and if the latter is true, if it is better to fit the mean values or to take the mean out of the fit parameters for every pixel.

## 5.1 Measurement of the ToT

The ToT for every single pixel is measured the same way as the threshold and noise in Chapter 4.1.2. In every 32<sup>nd</sup> pixel, different known charges are injected several times and the ToT is recorded. To configurate the electronics so that a m.i.p. signal results in a ToT of 30 BCU, the current source is adjusted either via IF for the whole FE chip or via FDAC for each pixel individually. This is done by injecting a charge equivalent to a m.i.p. signal and varying the DACs till the proper ToT is reached. After this, the ToT for several different charges is measured and recorded. These are the data used for the analysis.

## 5.2 Computational analysis of test data

The analysis is done with data of ToT for several charges for each pixel. The charge was injected by  $C_{low}$ . From the data the ToT for an injected charge  $Q_{inj}$  for each pixel can be derived. This is fitted with three functions that are:

1. Linear function:

$$\text{ToT} = m \cdot Q_{inj} + b$$

The fitting parameters are  $m$  and  $b$ . This function is motivated by the fact that the time the falling edge of the signal needs to decrease should be proportional to the injected charge. A constant is added because only a part of the falling edge is above the threshold.

2. Artificial function [8]:

$$\text{ToT} = P_1 + \frac{P_2}{P_3 + Q_{inj}} \quad (5.1)$$

The fitting parameters here are  $P_1$ ,  $P_2$  and  $P_3$ . This function is not derived from any physical equation. Despite of low values for ToT it describes the behaviour quite well. The function is currently used for the relation between ToT and charge. A sample fit is given in Fig. 5.2 to the left.

3. Function derived from triangle:

$$\text{ToT} = (Q_{inj} - \text{thres}) \cdot \left( \frac{t_1}{Q_{inj}} + \sqrt{\frac{1}{\cos^2 \alpha} - 1} \right) \quad (5.2)$$

## 5 Time over threshold analysis

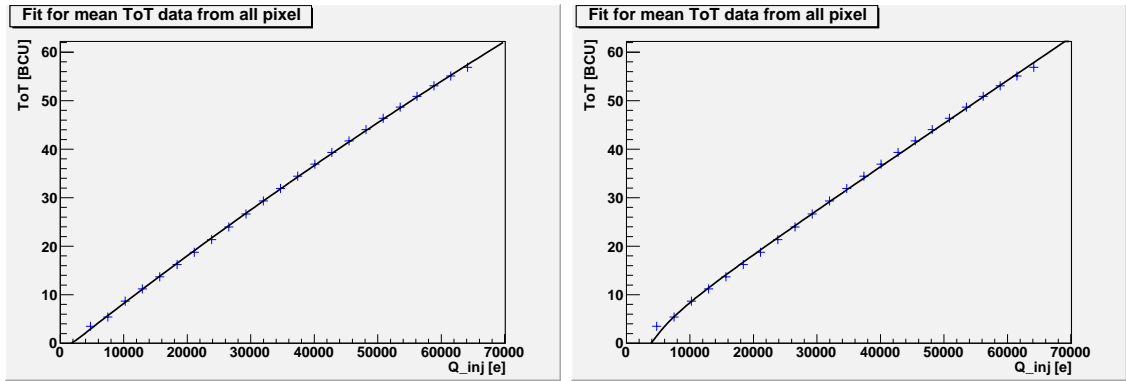


Figure 5.2: Graphs for function (5.1) (left) and function (5.2) (right) fitted on mean ToT-data of FE chip number 0 on module 510064.

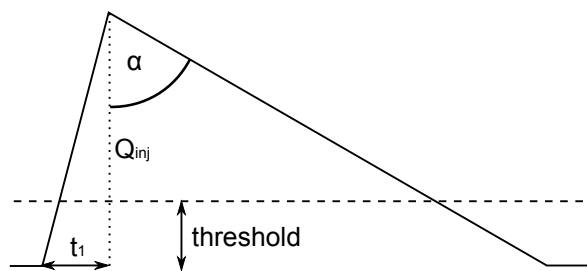


Figure 5.3: Fitting parameters in the charge triangle.

As the threshold is fixed at  $4000 e$  the fitting parameters are  $t_1$  and  $\alpha$ . This equation is derived from the assumption that the charge pulse has the shape of a triangle. The physical meanings of the parameters are illustrated in Fig. 5.3.  $t_1$  is the time needed for the charge pulse to reach its maximum and is normally around 1 BCU.  $\alpha$  represents the strength of the constant current. This is the parameter that is tuned to adjust the ToT to 30 BCU for a m.i.p.. A sample fit is given in Fig. 5.2 to the right.

There are two ways to fit the functions on the data. Either the data of each pixel is fitted and the mean values for the fit parameter are calculated or the data sets are added up and on this cumulative data one fit is performed. It should be noted that this is done for the pixels of one FE chip and not for the whole module as the fit parameters are relatively different for each FE chip.

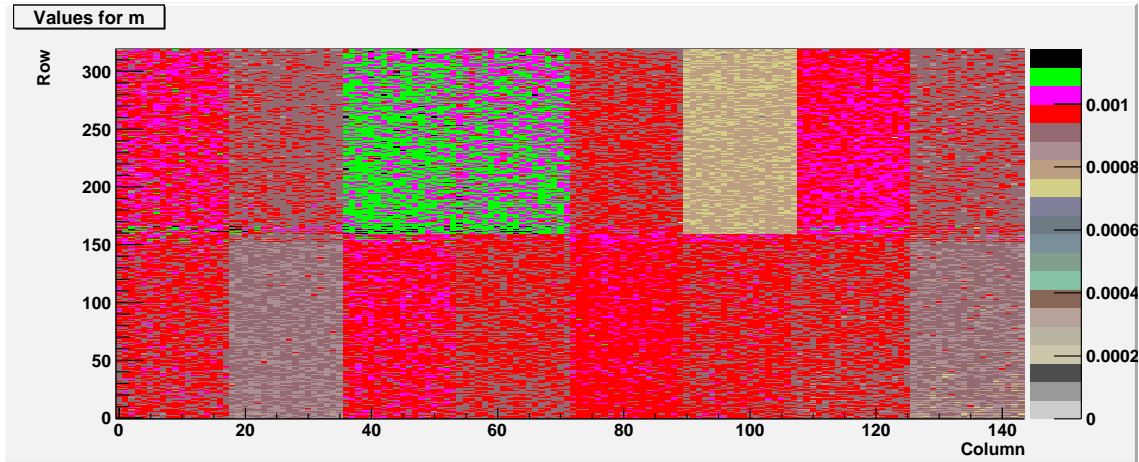


Figure 5.4: Fitting parameter  $m$  from linear fit for every pixel on the module.

## 5.3 Results

### 5.3.1 Module 510064 at FLEX stage

As the results of the analysis should not depend on the module only the module 510064 will be discussed extensively. A further restriction is that the fits will always be limited to one FE chip. The reason for this can be seen in Fig. 5.4. It shows the parameter  $m$  from a linear fit for every pixel on the module. For similar parameters for the whole module, the FE chips should not be seen as structures in the plot. But in fact the FE chips are relatively easy to see, which means that the mean values of the parameters on each FE chip are different. Most of the following analysis will be made on FE chip number 0, which is the one in the lower left corner.

The first thing is to test, which function fits the data best. So the ToT data for each pixel are fitted with the functions and the  $\chi^2$  is calculated via ROOT and divided by the degrees of freedom. Its mean values are:

$$\begin{aligned}\chi_{lin}^2/\text{NDF} &= 47.64 \\ \chi_{art}^2/\text{NDF} &= 12.63 \\ \chi_{tri}^2/\text{NDF} &= 26.91\end{aligned}$$

So the currently used artificial function is still better than the function derived from the shape of the charge pulse. The values of  $\chi^2/\text{NDF}$  for every pixel fit are illustrated in Fig. 5.5. It is clearly visible that not only the mean value is smaller

## 5 Time over threshold analysis

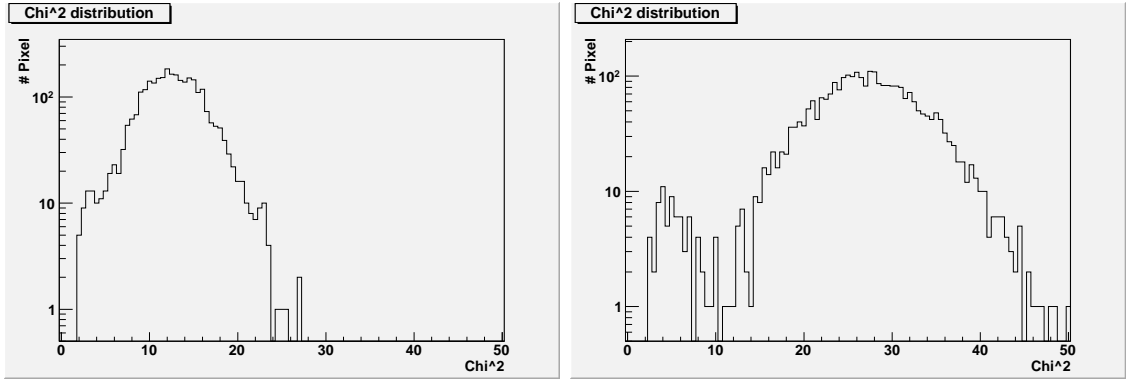


Figure 5.5:  $\chi^2/\text{NDF}$  for every pixel fitted with the artificial function (5.1) (left) and with function (5.2) (right).

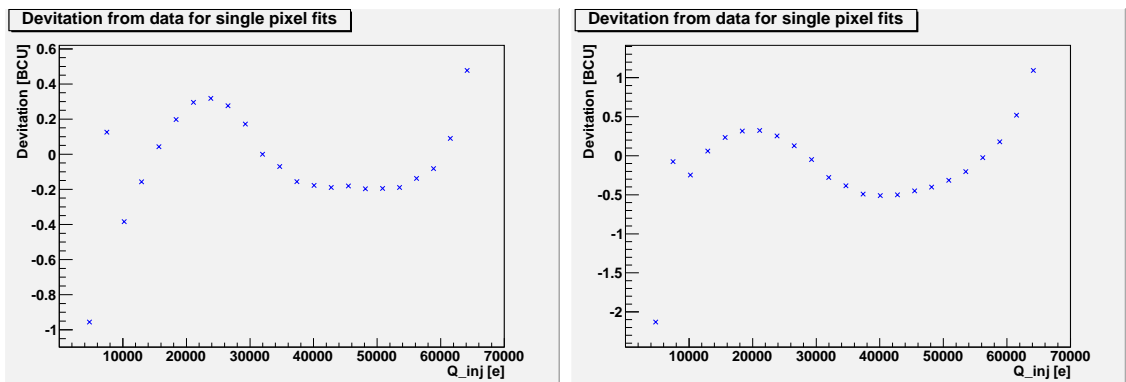


Figure 5.6: Deviation of the fits from the actual data. On the left for function (5.1) and on the right for (5.2).

for the artificial function, but also the spread of the values. However, the still high value for  $\chi^2/\text{NDF}$  shows that it the fit should still be optimized. As illustrated in Fig. 5.6, the fit tends to lie either over or under the ToT data for all chips. In this plot for every value of injected charge the deviation for the single pixel fits is added up and divided by the number of pixels. So if the ToT spreads statistically even around the fits, the net deviation should be near zero. But in fact the graph shows that the fit tends to be over the measured ToT for small charges below 20000  $e$  and to a smaller degree between 30000  $e$  and 60000  $e$ . In the other areas the fit tends to be slightly to low. The big difference between fit and data for small charges may result from the fact that not all injected pulses got over the threshold and thus the mean ToT might be more affected by noise than for higher charges. The same trends can be seen for the fit with function (5.2) but they are more distinct. Thus from now on only function (5.1) will be used.

Now it is interesting to know if one set of parameters for each FE chip is acceptable or if parameters for every single FE should be stored. There are two methods to gain a set of parameters for one FE chip. The first one just fits every pixel individually and then calculates the weighted mean for each parameter. The second one does this the other way round. It first calculates the weighted mean for the ToT data for all pixels and then fits it. To determine which method is better, the  $\chi^2/\text{NDF}$  for both sets of parameters are is calculated via

$$\chi^2/\text{NDF} = \frac{1}{n} \sum_{\text{all pixel}} \sum_{Q_{inj}} \frac{(\text{ToT}(Q_{inj}) - f(Q_{inj}))^2}{f(Q_{inj})}$$

with  $f(Q_{inj})$  being the expected ToT according to the fit function and  $n$  the degrees of freedom. The results are:

$$\begin{aligned} \chi_{\text{indiv}}^2/\text{NDF} &= 1873.24 \\ \chi_{\text{mean}}^2/\text{NDF} &= 127.39 \end{aligned}$$

So the method with fitting the mean ToT seems to be better. Compared to  $\chi_{\text{art}}^2$  it is about ten times as high. So it can be acceptable to store only one set of parameters for each FE chip, if storing and using sets for every individual pixel is too expensive in time or cost.

One should note, that the errors given for the ToT data are fairly low, as they derive only from the standard deviation of the original measurements. In the analysed data only the mean values of these measurements were given. When calculating the weighted average for the ToT for one module this leads to errors close to zero. The fit on these data has for example a  $\chi^2/\text{NDF} = 27892$ , which makes it impossible to draw a conclusion about the goodness of the fit.

### 5.3.2 Module 510064 at other stages

The only other stage at which the ToT scan for this module was done is ASSY. The mean  $\chi^2/\text{NDF}$  for the individual fits is:

$$\begin{aligned} \chi_{\text{lin}}^2/\text{NDF} &= 89.89 \\ \chi_{\text{art}}^2/\text{NDF} &= 25.40 \\ \chi_{\text{tri}}^2/\text{NDF} &= 55.91 \end{aligned}$$

## *5 Time over threshold analysis*

So the goodness of the fit is a bit worse here. However, the ranking of the fits does not change, not even the ratios change much.

On the other hand, the parameters change drastically. This is probably due to a different configuration of the whole module, i.e. a different sensor voltage. As the noise scan can be done even with the modules built in the detector, the parameters of the fit can be checked.

# 6 Conclusion

## 6.1 Analysis of bump bond connection quality

The analysis with noise from a depleted sensor and noise difference between depleted and undepleted sensor can detect a significant amount of unconnected pixels without losing too many connected ones. With exception of long ganged pixels for every pixel type, one of the two methods detects more than 80% of unconnected pixels while disabling least than 1% of the total number of pixels (see Tab. 4.2 and 4.4). The exception for long ganged pixels is no surprise, as 0.74% of these pixel are dead at STAVE stage. However, it is not possible to discriminate all unconnected pixels with these methods. So it is up to the operator to decide if it is better to have most unconnected pixels eliminated or to loose as few connected pixel as possible.

Setting different thresholds for each pixel type instead of one for all types increases the performance. Besides that, the limits for  $R_d$  and  $R_a$  respectively should also be set individually for each pixel type. For example unconnected long pixels are detected very well in a noise scan with a depleted sensor. At  $R_d = 80\%$ , the ratio of unconnected to connected pixels which are cut off is  $R_w = 14.02$ . So it is possible to increase  $R_d$  to 90% and more maintaining resonable values of  $R_a$  and  $R_w$ .

The modules with lead-tin can only be analysed with noise from a depleted sensor as they should have no noise with an undepleted sensor, if they are connected. However, only a little more than 25% of the unconnected pixels show noise (see Tab. 4.3). So dead pixels on these modules might be harder to detect.

Combining the two methods analysing the noise would most probably increase the efficiency even further. However, this needs some more research.

Methods to find merged pixel were only roughly sketched and should be further investigated.

## 6.2 Time over threshold analysis

The results were not as expected. Although the new function (5.2) is derived from the theoretical shape of the charge pulse, it fits the data not as well as the currently used artificial function (5.1). This means that most probably the shape of the pulse is not really a triangle. Instead, it is likely much smoother and the falling edge decreases not really linear.

Further analysis with the artificial function (5.1) has shown that one set of parameters for each FE chip could be acceptable. However, storing individual sets of parameters is clearly the better choice when high precision is needed.

How the parameters change over time and how function (5.2) can be improved needs additional research.

# Bibliography

- [1] ATLAS Collaboration. The ATLAS Experiment at the CERN Large Hadron Collider. *Journal of Instrumentation*, 3(08):S08003, 2008.
- [2] R.L. Glückstern. Uncertainties in track momentum and direction, due to multiple scattering and measurement errors. *Nuclear Instruments and Methods*, 24: 381 – 389, 1963. ISSN 0029-554X.
- [3] K. Kleinknecht. *Detektoren für Teilchenstrahlung*. Teubner, 2005.
- [4] W. R. Leo. *Techniques for Nuclear and Particle Physics Experiments A How-to Approach*. Springer-Verlag, 1994.
- [5] C. Amsler et al. Review of Particle Physics. *Physics Letters B*, 667(1-5):1 – 6, 2008. ISSN 0370-2693.
- [6] C. Grupen. *Teilchendetektoren*. BI Wissenschaftsverlag, 1993.
- [7] H. Spieler. *Semiconductor Detector Systems*. Oxford University Press, 2005.
- [8] J. Große-Knetter. *Vertex Measurement at a Hadron Collider - The ATLAS Pixel Detector*. Habilitation, Bonn University, March 2008.
- [9] G. Aad et al. Atlas pixel detector electronics and sensors. *Journal of Instrumentation*, 3(07):P07007, 2008.
- [10] I. Peric et al. The FEI3 readout chip for the ATLAS pixel detector. *Nuclear Instruments and Methods in Physics Research A*, 565:178187, 2006.
- [11] T. Stockmanns. *Multi-Chip-Modul-Entwicklung für den ATLAS-Pixeldetektor*. PhD thesis, Bonn University, 2004.
- [12] A. Andreazza, C. Gemme, J. Grosse-Knetter, A. F. Saavedra. *ATLAS Pixel Module Electrical Tests Description*, 2005. ATL-IP-QP-0144.
- [13] *ATLAS Trigger Performance Status Report*, 1998. CERN-LHCC-98-16.

## *Bibliography*

# Danksagung

Ich möchte an dieser Stelle allen danken, die - auf welche Art und Weise auch immer - zum Gelingen dieser Arbeit beigetragen haben.

Insbesondere möchte ich mich bei Jörn Grosse-Knetter bedanken, dafür dass er sich immer viel Zeit genommen hat mir bei meinen größeren Problemen zu helfen. Auch bei Nina Krieger möchte ich mich bedanken, dafür dass sie mir bei meinen Problemen mit ROOT geholfen, sowie diese Arbeit ausführlich Korrektur gelesen und sie mit vielen Anmerkungen bereichert hat.

Ich danke allen, die es mir ermöglicht haben meine Bachelorarbeit über einen Teil des ATLAS Detektors zu schreiben. Das war mit der Grund, warum ich angefangen habe dieses Fach zu studieren.

Nicht zuletzt möchte ich meinen Eltern danken, dass sie mir so ein sorgenfreies Studium ermöglichen. Danke!

**Erklärung** nach §13(8) der Prüfungsordnung für den Bachelor-Studiengang Physik und den Master-Studiengang Physik an der Universität Göttingen:

Hiermit erkläre ich, dass ich diese Abschlussarbeit selbständig verfasst habe, keine anderen als die angegebenen Quellen und Hilfsmittel benutzt habe und alle Stellen, die wörtlich oder sinngemäß aus veröffentlichten Schriften entnommen wurden, als solche kenntlich gemacht habe.

Darüberhinaus erkläre ich, dass diese Abschlussarbeit nicht, auch nicht auszugsweise, im Rahmen einer nichtbestanden Prüfung an dieser oder einer anderen Hochschule eingereicht wurde.

Göttingen, den 21. Juli 2009

(Lars Graber)